Extragalactic Magnetism with SOFIA (Legacy Program). I. The Magnetic Field in the Multiphase Interstellar Medium of M51[*]

Alejandro S. Borlaff[1] , Enrique Lopez-Rodriguez[2] , Rainer Beck[3], Rodion Stepanov[4] , Eva Ntormousi[5], Annie Hughes[6,7] , Konstantinos Tassis[8,9] , Pamela M. Marcum[1], Lucas Grosset[2], John E. Beckman[10,11], Leslie Proudfit[12], Susan E. Clark[13] , Tanio Díaz-Santos[14], Sui Ann Mao[3], William T. Reach[12] , Julia Roman-Duval[15] , Kandaswamy Subramanian[16], Le Ngoc Tram[12] , Ellen G. Zweibel[17,18] , and Daniel Dale[19]

Legacy Team

[1] NASA Ames Research Center, Moffett Field, CA 94035, USA; a.s.borlaff@nasa.gov
[2] Kavli Institute for Particle Astrophysics & Cosmology (KIPAC), Stanford University, Stanford, CA 94305, USA
[3] Max-Planck-Institut für Radioastronomie, Auf dem Hügel 69, D-53121 Bonn, Germany
[4] Institute of Continuous Media Mechanics, Korolyov str. 1, 614013 Perm, Russia
[5] Scuola Normale Superiore, Piazza dei Cavalieri 7, I-56126 Pisa, Italy
[6] CNRS, IRAP, 9 Av. du Colonel Roche, BP 44346, F-31028 Toulouse cedex 4, France
[7] Universite de Toulouse, UPS-OMP, IRAP, F-31028 Toulouse cedex 4, France
[8] Institute of Astrophysics, Foundation for Research and Technology-Hellas, 71110 Heraklion, Greece
[9] Department of Physics, and Institute for Theoretical and Computational Physics, University of Crete, 70013 Heraklion, Greece
[10] Instituto de Astrofísica de Canarias, C/Via Láctea s/n, E-38200 La Laguna, Tenerife, Spain
[11] Departamento de Astrofísica, Universidad de La Laguna, Avda. Astrofísico Fco. Sánchez s/n, E-38200 La Laguna, Tenerife, Spain
[12] SOFIA Science Center, NASA Ames Research Center, Moffett Field, CA 94035, USA
[13] Institute for Advanced Study, 1 Einstein Drive, Princeton, NJ 08540, USA
[14] Institute of Astrophysics, Foundation for Research and Technology-Hellas (FORTH), Heraklion, 70013, Greece
[15] Space Telescope Science Institute, 3700 San Martin Drive, Baltimore, MD 21218, USA
[16] Inter-University Centre for Astronomy and Astrophysics, Post Bag 4, Ganeshkhind, Pune 411007, India
[17] Department of Astronomy, University of Wisconsin–Madison, 475 North Charter Street, Madison, WI 53706, USA
[18] Department of Physics, University of Wisconsin–Madison, 1150 University Avenue, Madison, WI 53706, USA
[19] Department of Physics & Astronomy, University of Wyoming, Laramie, WY 82070, USA

Abstract

The recent availability of high-resolution far-infrared (FIR) polarization observations of galaxies using HAWC +/SOFIA has facilitated studies of extragalactic magnetic fields in the cold and dense molecular disks. We investigate whether any significant structural differences are detectable in the kiloparsec-scale magnetic field of the grand design face-on spiral galaxy M51 when traced within the diffuse (radio) and the dense and cold (FIR) interstellar medium (ISM). Our analysis reveals a complex scenario where radio and FIR polarization observations do not necessarily trace the same magnetic field structure. We find that the magnetic field in the arms is wrapped tighter at 154 μm than at 3 and 6 cm; statistically significant lower values for the magnetic pitch angle are measured at FIR in the outskirts ($R \geqslant 7$ kpc) of the galaxy. This difference is not detected in the interarm region. We find strong correlations of the polarization fraction and total intensity at FIR and radio with the gas column density and ^{12}CO(1–0) velocity dispersion. We conclude that the arms show a relative increase of small-scale turbulent B-fields at regions with increasing column density and dispersion velocities of the molecular gas. No correlations are found with H I neutral gas. The star formation rate shows a clear correlation with the radio polarized intensity, which is not found in FIR, pointing to a small-scale dynamo-driven B-field amplification scenario. This work shows that multiwavelength polarization observations are key to disentangling the interlocked relation between star formation, magnetic fields, and gas kinematics in the multiphase ISM.

Unified Astronomy Thesaurus concepts: Spiral galaxies (1560); Extragalactic magnetic fields (507); Magnetic fields (994); Star formation (1569); Molecular clouds (1072); Far infrared astronomy (529); Radio astronomy (1338); Polarimetry (1278)

1. Introduction

Pioneering optical polarimetric observations in galaxies detected the interstellar polarization due to aligned dust grains, which motivated the discussion of magnetic fields (*B*-fields) in galaxies (i.e., Elvius 1951; Aller 1958; Elvius & Hall 1964; Piddington 1964; Segalovitz et al. 1976; Scarrott et al. 1987). The

formation and sustainability of *B*-fields in the galactic disks, as well as their possible role in the evolution of their hosts, are still outstanding questions of modern astrophysics. Primordial magnetic fields are not strong enough (Rees 1987; Gnedin et al. 2000; Subramanian 2016) to explain the observations in spiral galaxies by simple gravitational collapse (Beck et al. 1996). Extragalactic *B*-fields are thought to be generated by galactic dynamos, which rely on small-scale turbulent velocity fields and differential rotation of the galactic disk to amplify and order the *B*-fields (i.e., Beck et al. 1996; Gressel et al. 2008a, 2008b; Gent et al. 2012; Bendre et al. 2015). Current dynamo theories can be divided into

---

large-scale dynamos, which produce regular B-fields on scales larger than the flow scale, and small-scale dynamos, generated at scales smaller than the energy-carrying eddies (Rees 1987; Gnedin et al. 2000; Brandenburg & Subramanian 2005; Gressel et al. 2008a, 2008b; Subramanian 2016). The coherence length scale of supernova-driven turbulence is 50–100 pc (i.e., Haverkorn et al. 2008). The most prominent theory for large-scale dynamos is given by the mean-field approach, where the velocity and B-fields are decomposed into averaged and fluctuating components, whose average can either be an ensemble average or some kind of spatial average (Brandenburg et al. 2012). Recently, more attention has been given to small-scale dynamos, as they are more generic in terms of flow Requirements and exhibit much faster B-field growth. The amplification timescale of small-scale B-fields is of the order of the smallest turbulent eddy turnover timescale. This is important because the small-scale dynamos allow amplification of the B-fields even in galaxy clusters or elliptical galaxies (Brandenburg & Subramanian 2005; Sur et al. 2021). The small-scale B-fields may also explain the strong B-fields in high-redshift galaxies when the universe was much younger and large-scale dynamo amplification times were not sufficient (Arshakian et al. 2009).

The dynamical role of magnetic fields on galactic scales is strongly debated. Magnetic fields in galaxies are strong enough to turn a significant amount of kinetic energy into magnetic energy, driving gas mass inflows into the galactic core (Kim & Stone 2012). Magnetic fields have even been considered as a hidden contributor to flattening rotation curves (Battaner & Florido 2007; Ruiz-Granados et al. 2010, 2012; Tsiklauri 2011; Jałocha et al. 2012a, 2012b). However, various studies have posited that the local conditions of magnetic fields might be too turbulent to add significant kinematic support to the gas disk or create a systematic stellar migration (Sánchez-Salcedo & Santillán 2013; Elstner et al. 2014). In spite of these arguments, recent magnetohydrodynamic simulations of Milky Way–mass objects with magnetic fields have shown that the resulting galaxies present more extended disks, showing more gas and atomic hydrogen in their halos than those models without them (van de Voort et al. 2021). Tabatabaei et al. (2016) found a correlation between the large-scale magnetic field strength and the rotation speed of galaxies showing the effect of the gas dynamics in ordering the magnetic fields in galaxies. Different authors considered that these B-fields are able to significantly influence disk galaxies, dominating the fragmentation pattern (Körtgen et al. 2019) and affecting the global rotation of the gas (Martin-Alvarez et al. 2020).

Most of our knowledge about extragalactic magnetism comes from radio polarimetric observations (i.e., Mathewson et al. 1972; Vollmer et al. 2013; Beck 2015a; Krause et al. 2020) by means of synchrotron polarized emission from energetic particles in the diffuse interstellar medium (ISM) and intergalactic medium (IGM). Using a sample of 13 galaxies from the CHANG-ES radio continuum survey, Krause et al. (2018) found that the 4–30 cm radio observations are sensitive to average scale heights of 1–2 kpc. Synchrotron emission measures the total magnetic field strength and the magnetic field component in the plane of the sky (POS), while the magnetic field component along the line of sight (LOS) is inferred using the effect of Faraday rotation. Synchrotron polarization provides a measurement of the degree of order of

the B-field, where the ordered field can be a regular (dynamo-generated) and/or an anisotropic turbulent one. The fractional polarization can decrease due to beam, bandwidth, and/or wavelength-dependent depolarization. Beam depolarization occurs due to tangled B-fields within the beam size of the observations. Bandwidth depolarization arises from the rotation of the plane of polarization at different frequencies within the frequency range of the observations. Wavelength-dependent depolarization is caused by Faraday rotation along the LOS or within the source. Major efforts have been performed to estimate the B-field orientation of galaxies using optical (Elvius 1951; Elvius & Hall 1964; Scarrott et al. 1987; Fendt et al. 1998) and near-IR (NIR; Jones 1997, 2000; Pavel & Clemens 2012) polarization techniques via dichroic absorption. However, dust/electron scattering seems to be the dominant polarization mechanism in some of these observations, where after careful subtraction, the B-field can be inferred (i.e., M82, Jones 1997, 2000).

Magnetic fields in galaxies have also been measured using thermal emission from magnetically aligned dust grains at far-IR (FIR; Lopez-Rodriguez et al. 2018, 2020, 2021; Jones et al. 2019, 2020; Lopez-Rodriguez 2021) and submillimeter (850 μm) wavelengths (i.e., Greaves et al. 2000; Matthews et al. 2009). These studies have shown that the FIR wavelength range (50–220 μm) can characterize the strength and structure of B-fields in galaxies. The FIR polarimetric observations of the edge-on galaxies Centaurus A (Lopez-Rodriguez 2021), M82 (Jones et al. 2019; Lopez-Rodriguez et al. 2021), NGC 253 (Jones et al. 2019), and NGC 891 (Jones et al. 2020) show scale heights <500 pc for the galactic disks. At these wavelengths, the spectral energy distribution of galaxies is dominated by the thermal emission from interstellar dust at temperatures of 10–100 K, which traces deeper regions of the molecular disk than those from optical, NIR, and radio. Dust grains have their long axes aligned perpendicular to the local B-field, as described by the radiative torque alignment theories (RATs; i.e., Hoang & Lazarian 2014; Andersson et al. 2015). Thus, thermal polarized emission measures the B-field orientation in the POS after the polarization angles are rotated by 90°. As in radio wavelengths, thermal polarization provides a measurement of the degree of order of B-fields. The thermal polarization fraction is affected by beam depolarization, turbulence at scales smaller than the observational beam, and physical properties of the dust grains including temperature, column density, and alignment efficiency.

The ISM of the spiral galaxies is highly heterogeneous. The cold and dense clouds and the diffuse ISM (Field et al. 1969) dominate different regions of the galactic disk. Molecular gas is closer to the galactic plane, while the scale height of the diffuse ISM can be 1 order of magnitude larger (Ferrière 2001). Molecular gas also is more rotationally supported than the diffuse ionized gas component, which has higher dispersion in velocity (Davis et al. 2013; Levy et al. 2018). As most of the studies of kiloparsec-scale magnetic fields in galactic disks are based on radio polarimetric observations, our knowledge is mainly focused on the B-field tracing the diffuse ISM, rather than the cold dense molecular clouds and filaments. However, it is inside the molecular clouds where star formation takes place and turbulence and magnetic fields can be dominant forces (Santos et al. 2016; Pillai 2017; Pillai et al. 2020). The geometry of the magnetic field in observations of Galactic polarized dust emission suggests that the magnetic field

structure may influence the formation of molecular clouds. The magnetic field is aligned preferentially parallel to molecular cloud structures at low densities, preferentially perpendicular at higher densities, and back to parallel at even higher densities (Planck Collaboration et al. 2016; Soler et al. 2017; Fissel et al. 2019).

Using the High-resolution Airborne Wideband Camera-plus (HAWC+; Vaillancourt et al. 2007; Dowell et al. 2010; Harper et al. 2018) installed on the 2.7 m Stratospheric Observatory for Infrared Astronomy (SOFIA) FIR polarization observations, Pillai et al. (2020) found evidence for a multiphase processing scenario where gas filaments merge into a central region in the molecular clouds, reorienting the magnetic field in dense gas flows compared to the orientation of the surrounding ISM. These transitions in the orientation of the magnetic fields may be related to small-scale gas accretion kinematics and the subsequent magnetic field line dragging, as reported by magnetohydrodynamic simulations (Gómez et al. 2018). The morphological and kinematic differences between the diffuse ISM and the molecular clouds elicit a basic, yet unresolved, question: how does the multiphase ISM in galaxies affect the B-field? Motivated by the potentially important role of magnetic fields in the dense ISM, we quantify the morphology and degree of order of the B-field in the multiphase ISM traced by FIR and radio polarimetric observations.

Given that polarization studies are strongly limited by the signal-to-noise ratio (S/N), local bright galaxies are the most extensively studied objects. One of these objects is the grand design face-on spiral M51. Although there have been attempts to measure the B-field in M51 using optical (Scarrott et al. 1987) and NIR (Pavel & Clemens 2012) wavelengths, these observations have been found to be dominated by dust/electron scattering. The kiloparsec-scale B-field of M51 has been traced using radio polarimetric observations (Mathewson et al. 1972; Beck et al. 1987; Horellou et al. 1992; Neininger 1992; Patrikeev et al. 2006; Fletcher et al. 2011; Kierdorf et al. 2020). These studies have shown an ordered kiloparsec-scale B-field where turbulent B-fields dominate in the arms, while a regular B-field dominates in the interarm. In addition, Kierdorf et al. (2020) measured that the turbulent B-field strength and/or thermal electron density decrease toward larger radii. In a recent study, Jones et al. (2020) presented the inferred B-field orientation of M51 traced by 154 μm thermal emission of magnetically aligned dust grains using HAWC+/SOFIA. The authors showed the general B-field structure of the disk and compared it with results from previous radio polarization observations at 6 cm (Fletcher et al. 2011). The authors concluded that the magnetic fields traced in radio and FIR have a similar general structure showing no obvious differences on inspection by eye.

Detecting systematic differences in the magnetic field between radio and FIR wavelengths requires precise and quantitative statistics to be estimated using both data sets. Since the star formation rate (SFR) is not homogeneous across the galactic disks of spiral galaxies, variances between the polarization maps at radio and FIR would be expected to likewise have an inhomogeneous spatial distribution as the multiphase ISM affects the galactic B-field. Thus, our investigation is particularly focused on the radial variation and differences between disk regions (arms versus interarm). In the particular case of M51, we also look for a possible variation of the magnetic field orientation between the northern region (closer to the interacting companion M51b) and the southern section. In this paper, we revisit the magnetic field structure of M51, using deeper observations than those presented by Jones et al. (2020), to quantitatively investigate how the properties of M51's magnetic field structure correlate with wavelength, morphological region, and ISM phase.

The paper is organized as follows. We describe the different data sets used to study the multiphase ISM, the morphology of the galaxy for different tracers, and the magnetic structure of M51 in Section 2. We present the statistical methods used to parameterize them in Section 3. Section 4 is dedicated to the analysis of the magnetic and morphological spiral structure of M51. In Section 5, we analyze the properties of the ISM of M51 as a function of the column density, FIR and radio polarization, and gas kinematics for multiple phases of the galactic gaseous disk. Finally, Sections 6 and 7 contain the discussion and conclusions, respectively. In this paper, we assume a distance to M51 of 8.58 ± 0.28 Mpc ($1'' \sim 41.6$ pc), based on the results from McQuinn et al. (2017) from the analysis of the tip of the red giant branch.

2. Archival Data

2.1. FIR Polarimetry

Publicly available SOFIA/HAWC+ observations of M51 obtained under proposals with IDs 70_0509 (Guaranteed Time Observations by the HAWC+ Team), 76_0003 (Discretionary Director Time), and 08_0260 (PI: D. Dowell) from 2017 to 2020 (see Figure 1) were used. Table 1 summarizes the observations combined in this work. Polarimetric observations with HAWC+ simultaneously measure two orthogonal components of linear polarization in two arrays of 32 × 40 pixels each. Observations were performed using Band D with a characteristic central wavelength of 154 μm, bandwidth of 34 μm, pixel scale of 6.″90, and beam size (FWHM) of 13.″6 (Harper et al. 2018). For M51, $\text{FWHM}_{\text{HAWC+}} = 0.565$ kpc. Observations were performed in a four-position dither square pattern with a distance of several detector pixels in the equatorial sky coordinates system (ERF) as shown in Table 1 (column 8). The ERF for these observations was used, so a positive increase of angles is in the counterclockwise direction. In each dither position, four half-wave plate (HWP) position angles (PAs) were taken in the standard sequence 5°, 27°.5, 50°, and 72°.5. These dither sequences of four HWP PAs will be referred to as "sets" hereafter. A chop frequency of 10.2 Hz was used, with the chop angle, chop throw, and nod time as listed in Table 1. The chop angle is defined as the angle in the east-of-north direction along which the telescope chops with a given chop throw.

The total observation time (on-source time + overheads) is 7.21 hr, of which 2.78 hr is the time on-source. Low-quality exposures due to bad tracking, vignetting by the observatory's door in flight F547, or other technical issues at the time of observations are listed in parentheses in the sets column. The observations require time on the off position due to the chop-nod technique, as well as time to take internal calibrators right before and after each set of four HWP PAs, which translates to an overhead of approximately × 2.6. Note that the previously published results of M51 by Jones et al. (2020) used only a subset of the data presented here. Specifically, Jones et al. (2020) used observations from 70_0509 and 76_0003, with a total time of 4.6 hr, where our observations encompass a total
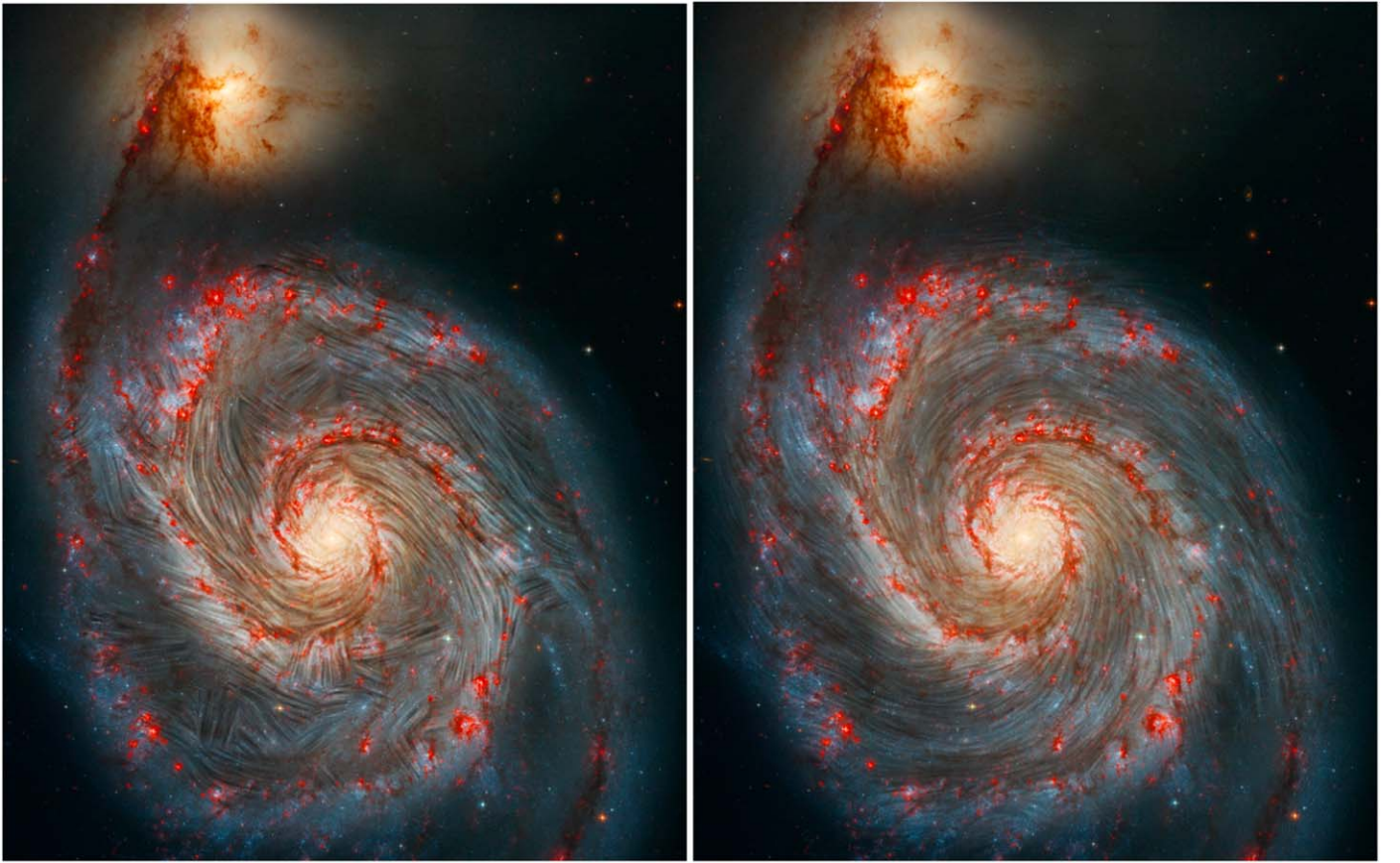
Figure 1. The FIR (154 μm from this work; left) and radio polarization (6 cm from Fletcher et al. 2011; right) magnetic field orientation in the POS represented over the optical morphology of M51. The RGB background shows the Hubble Space Telescope observations of M51 with the F658N (Hα) and F814W (red), F555W (green), and F435W (blue) bands using the Advanced Camera for Surveys. The overlaid stripped texture shows how the LIC (Cabral & Leedom 1993) technique was used to show the orientations of the B-field at FIR and radio, where only polarization measurements with $P/\sigma_P \geqslant 3$, a resample scale of 5, and a contrast of 2 was used.

Table 1
Summary of HAWC+ Polarimetric Observations

PlanID	Date (YYYYMMDD)	Flight ID	Altitude (ft)	Chop Angle (deg)	Chop Throw (arcsec)	Nod Time (s)	Dith. Scale (arcsec)	No. Sets (Bad)	t_{obs_time} (s)
(1)	(2)	(3)	(4)	(5)	(6)	(7)	(8)	(9)	(10)
70_0509	20171109	F450	43,000	105	400	40	20	6	1263
						50	33	4	1003
						35	33	3	573
	20101115	F452	43,000	105	400	40	33	7(2)	1495
							35	8	1696
						35	35	3	575
	20171117	F454	43,000	105	400	40	33	10	2122
76_0003	20190212	F545	42,000	90	450	45	20	8	1852
	20190220	F547	43,000	90	450	50	20	8	2135
							27	4(4)	1338
08_0260	20200118	F651	43,000	105	450	50	20	17	4200
							28	8	1993
	20200125	F653	43,000	105	450	50	20	8(1)	1993
							28	15	3715

Note. Columns: (1) observation plan identifier, (2) observation date, (3) flight ID, (4) sea-level altitude during the observations (feet), (5) chop angle (degrees), (6) chop throw (arcseconds), (7) time between nodding iterations (seconds), (8) amplitude of the dithering pattern (arcseconds), (9) number of observation sets obtained (and rejected), (10) total observation time (on-source + overheads; seconds).

observing time of 7.21 hr. We present here observations with a larger integration time and better sensitivity, which allow us to perform a quantitative analysis of the inner and outer arms of M51. In addition, our data reduction pipeline, supported by the SOFIA Science Center, is the most updated version (v2.3.2), in comparison with that used by Jones et al. (2020), v1.3.0beta3. The new pipeline version corrects for background subtraction and propagation of errors from the time streams, so no inflated errors using a χ^2 analysis are required, and smoothing techniques have been implemented to account for correlated
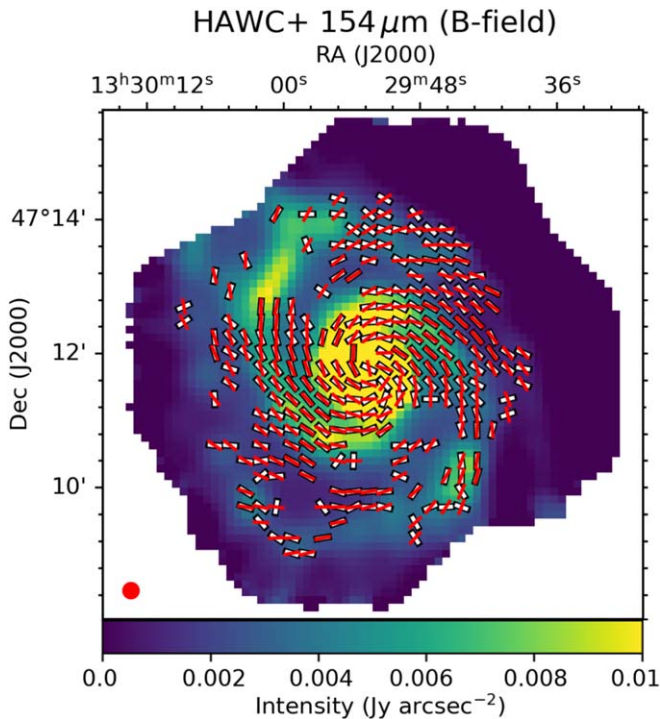
Figure 2. *B*-field orientation maps of M51 from 154 μm/HAWC+ (this work) polarimetric observations. The white lines represent the *B*-field orientations, where the lengths have been normalized to unity. Red lines are the average polarization orientation estimated from the magnetic pitch angle profile. The background color map represents the total surface brightness intensity in their respective wavelengths.

pixels. A direct comparison between both data sets is beyond the scope of this manuscript, and we refer the reader to the update of the pipeline by the SOFIA Science Center for further details.

The observations were reduced using the HAWC_DRP_PIPE-LINE V2.3.2. The pipeline procedure described by Harper et al. (2018) was used to background-subtract and flux-calibrate the data and compute Stokes parameters and their uncertainties. The final degree and PA of polarization are corrected for instrumental polarization, bias, and polarization efficiency. Typical standard deviations of the degree of polarization after subtraction of $\sim$0.8% are estimated. We generated final reduced images with a pixel scale equal to the half-beam size, which corresponds to $6\farcs8$. Further analysis and high-level displays were performed with custom PYTHON routines, described in Section 3.1. We discard all of those measurements with an S/N lower than 2 in polarized intensity ($p_{\lim}=0.05$, probability higher than 95% of having a signal higher than the noise level) in order to avoid regions dominated by noise. We also discard those pixels with an S/N in total intensity lower than $\sqrt{2}/p_{\lim}\sim28.28$. We refer the reader to Section 4 of Gordon et al. (2018) for more details on SOFIA/HAWC+ quality cuts. The inferred *B*-field orientation at 154 μm is shown as streamlines using the line integral convolution (LIC; Cabral & Leedom 1993) technique in Figure 1 (left panel), where only polarization measurements with $P/\sigma_P \geqslant 3$ were used, with σ_P as the uncertainty in the polarization fraction. A resample scale of 5 and a contrast of 2 were used to compute the LIC image. The total intensity and polarization map is shown in Figure 2. Inferred *B*-field orientations and the SOFIA/HAWC+ footprint at 154 μm are shown in Figure 4.

In all figures, the observed PAs of polarization have been rotated by 90°. These observations are used to trace the magnetic fields in the cold and dense ISM regions of M51.

2.2. Radio Polarimetry

We make use of the 3 and 6 cm radio polarimetric maps at a resolution of $8''$ from Fletcher et al. (2011). These data sets were obtained using a combination of observations from the Karl G. Jansky Very Large Array (VLA) and the Effelsberg 100 m single-dish radio telescopes. We refer to the original paper for a complete description of the observations and data reductions of the data sets used in our work. Longer-wavelength (18 and 20 cm) observations from Fletcher et al. (2011) can be strongly affected by Faraday rotation (Beck & Wielebinski 2013) and are thus not considered in this work. For our analysis, Stokes *IQU* were convolved with a Gaussian kernel to match an $\mathrm{FWHM_{HAWC+}} = 13\farcs6$ and reprojected to the HAWC+ observations. Then, the degree and PA of polarization and polarized flux were computed, accounting for the level of polarization bias as a function of the S/N (Wardle & Kronberg 1974). We show the magnetic field streamlines of the 6 cm data set in Figure 1 (right panel), compared to those of the 154 μm/HAWC+ observations (left panel). A resample scale of 5 and a contrast of 2 were used to compute the LIC image. Final inferred *B*-field orientations at 3 and 6 cm are shown in Figure 3 (left and right panels, respectively), where the observed PAs of polarization have the same length. To avoid biased results due to the number of measurements across the galaxy, we only use radio polarization measurements that are spatially coincident with the HAWC+ observations. The radio polarization maps are used to spatially correlate the polarization arising from synchrotron emission with that arising from thermal emission by means of magnetically aligned dust grains observed with HAWC+, as detailed in Section 4.

2.3. CO and H I Observations

The ^{12}CO(1–0) observations were obtained from the Plateau de Bure interferometer (PdBI) and Arcsecond Whirlpool Survey (PAWS[20]), which uses the PdBI and IRAM 30 m data to image the emission from the molecular gas disk in M51 at high angular resolution. The data are described in Pety et al. (2013) and Colombo et al. (2014). Specifically, we used moments 0 (integrated emission line) and 2 (intensity-weighted dispersion, velocity dispersion) of the ^{12}CO(1–0) emission line at angular resolutions of $6''$. For our analysis, moments 0 and 2 were convolved using a Gaussian kernel to match the HAWC+ beam size of $13\farcs6$ and then reprojected to the grid of the HAWC+ observations. The H I data were obtained from The H I Nearby Galaxy Survey (THINGS[21]), described in Walter et al. (2008). Moments 0 and 2 were used to trace the neutral gas in the disk of M51. For our analysis, these observations were processed using the same method as the ^{12}CO(1–0) observations.

Both the ^{12}CO(1–0) and H I data sets are used to trace the velocity dispersion as a proxy of the turbulence in the molecular and neutral gas. We note that the ^{12}CO(1–0) integrated emission-line images of IRAM 30 m at a resolution of $23''$ cover the full field of view (FOV) of the HAWC+ observations. However, due

---

[20] The PAWS data are at https://www2.mpia-hd.mpg.de/PAWS/PAWS/Home.html.
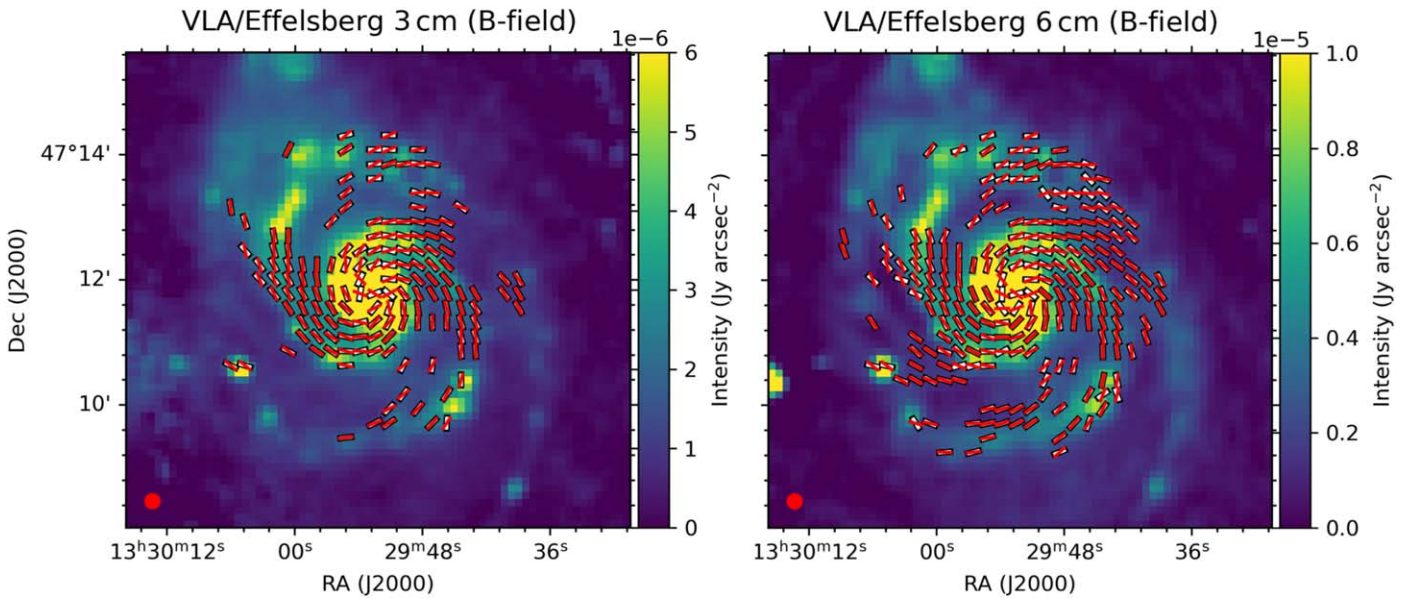[21] THINGS project: https://www2.mpia-hd.mpg.de/THINGS/Data.html.

Figure 3. The B-field orientation maps of M51 from radio polarimetric observations at 3 (left) and 6 cm (right; Fletcher et al. 2011). The white lines represent the B-field orientations, where the lengths have been normalized to unity. Red lines are the average polarization orientation estimated from the magnetic pitch angle profile. The background color map represents the total surface brightness intensity in their respective wavelengths.

to the low angular resolution of the IRAM 30 m observations, any comparison between structures of the galaxy (arms, interarms) and polarization observations are not physically meaningful, as the structures are hardly distinguished. In addition, we used THINGS H I 21 cm data sets to generate the morphological mask that separates the arm and interarm regions (see Section 3.3).

2.4. Column Density Map

The column density map, $N_{\rm H\,I+2H_2}$, was estimated using the integrated emission-line (moment 0) neutral, H I, and molecular ^{12}CO(1–0) gas of M51. The IRAM 30 m ^{12}CO(1–0) integrated emission-line observations with a resolution of 23″ were used for this analysis. These observations cover the full FOV of the HAWC+ observations, while the 6″ observations used in Section 2.3 only cover the central $\sim$3′ of M51. Specifically, we used the following H I and ^{12}CO(1–0) conversions to $N_{\rm H\,I}$ and $N_{\rm 2H_2}$:

$$N_{\rm H\,I} = 1.105 \times 10^{21} \frac{I_{\rm H\,I}}{\rm FWHM_{HAWC+}^2} \ (\rm cm^{-2}) \qquad (1)$$

by Hunter et al. (2012), where $I_{\rm H\,I}$ is the integrated emission line (moment 0) of H I in units of Jy beam^{-1} m s^{-1}, and FWHM$_{\rm HAWC+}$ is the beam size of HAWC+ at 154 μm in units of arcseconds; and

$$N_{\rm 2H_2} = X_{\rm CO} I_{\rm CO} \ (\rm cm^{-2}) \qquad (2)$$

by Bolatto et al. (2013), where $I_{\rm CO}$ is the integrated emission line (moment 0) of ^{12}CO(1–0) in units of K km s^{-1}, and $X_{\rm CO}$ is the conversion factor of value 2×10^{20} cm^{-2} (K km s^{-1})$^{-1}$.

The final column density is estimated as $N_{\rm H\,I+2H_2} = N_{\rm H\,I} + N_{\rm 2H_2}$. Column density values are in the range $\log_{10}(N_{\rm H\,I+2H_2}[\rm cm^{-2}]) = [20.4–22.11]$, in agreement with Mentuch Cooper et al. (2012). The computed column density is used for the analysis of the multiphase ISM, as well as the estimation of the SFR.

3. Methods

3.1. Magnetic and Morphological Pitch Angle Analysis

In this section, we describe the methodology used to estimate the magnetic and morphological pitch angles of M51. The algorithm described here is used to analyze the FIR, radio polarimetric observations, and velocity fields that result from the wavelet analysis of their total intensity maps (see Section 3.2).

The magnetic pitch angle profile is estimated as follows.

1. The debiased polarization level and its associated uncertainty are computed using the Stokes IQU parameters and their uncertainties δI, δQ, δU:

$$P_{\rm debias} = \sqrt{P^2 - \delta P^2}, \qquad (3)$$

where

$$P = \sqrt{\left(\frac{Q}{I}\right)^2 + \left(\frac{U}{I}\right)^2} \qquad (4)$$

and

$$\delta P = \frac{1}{I}\sqrt{\frac{(Q \cdot \delta Q)^2 + (U \cdot \delta U)^2}{Q^2 + U^2} + \delta I^2 \frac{Q^2 + U^2}{I^2}}. \qquad (5)$$

2. To reproject the observations, our method requires the coordinates of the galactic center (α, δ); the galactic disk inclination, i; and tilt angle, θ. Morphological parameters were adopted from Colombo et al. (2014) and have the following values: $\alpha = 202°.4699$, $\delta = +47°.1952$, $i = 22° \pm 5°$, and $\theta = -7°.0 \pm 3°.0$, where α and δ are the equatorial coordinates of the center of M51, i is the apparent inclination of the disk with the LOS (where face-on corresponds to $i = 0°$), and θ is the apparent tilt angle of the major axis with positive values in the east-of-north direction (where north corresponds to $\theta = 0°$).

3. We compute the radius (R) and azimuthal position (ϕ) of every pixel in galactocentric coordinates, where all pixels

are assumed to be located in the galactic plane ($z = 0$). Radial and angular masks are generated with the same tilt angle and inclination as M51.

4. An azimuthal angular mask is created. This is generated such that the deprojected vector at each pixel location is perpendicular to the radial direction. We will refer to this idealized field as the "zero pitch angle" field, or Ξ. The observed debiased polarization measurements (P_{debias}) are deprojected to the galactic plane frame (P') using two chained rotation matrices, one to account for the inclination of the galaxy, $R_x[i]$, and a second for the tilt angle, $R_z[\theta]$. The projected matrix is estimated to be $P' = R_x[i]R_z[\theta]P$.

5. A method was devised to account for the 180° degeneracy in the direction of HAWC+'s PAs. An effective averaging of the directions of several pixels requires resolution of the degeneracies. The Ξ zero pitch angle frame from the previous step is used to correct the PAs, arbitrarily setting them to a common outward-pointing direction. This is performed by measuring the relative angle difference with Ξ and adding or subtracting 180° as required. Note that the result is independent of the reference angle of choice, and it is only used for averaging purposes. As a consequence of this correction, the magnetic pitch angle profile also suffers a 180° degeneracy.

6. We project the measured B-field orientations to a new reference frame in which the galaxy is observed face-on. We used the morphological parameters of the inclination and tilt angles (i, θ) and the measured PAs of the B-field orientation corrected for 180° degeneracy from the previous step.

7. The pitch angle $\Psi(x, y)$ is calculated as the difference between the measured PAs of the B-field orientation and the Ξ vector field.

8. Then, $\Psi(x, y)$ is averaged at each radius from the core. The radial bins are linearly spaced, and the number of them is optimized as a compromise between S/N and spatial resolution. The angular average is performed as follows:

$$\overline{\Psi}(R) = \mathrm{atan2}\left(\frac{<\cos \Psi(x, y)>}{<\sin \Psi(x, y)>}\right), \qquad (6)$$

where the $<>$ operator indicates a robust median value (based on Monte Carlo simulations) and $\overline{\Psi}(R)$ is the averaged magnetic pitch angle value for a certain radial bin. For each map, the process detailed below is repeated 10,000 times, using Monte Carlo simulations to include the uncertainties of the tilt angle, inclination, and Stokes parameters. An independent Gaussian probability distribution for each parameter is assumed, with a standard deviation σ equal to their uncertainties. Each of these Monte Carlo simulations produces a magnetic pitch angle array. The results of the Monte Carlo simulations are stored in a data cube, which are later used to calculate the pitch angle profiles ($\overline{\Psi}(R)$). Finally, for each radial bin, the median $\overline{\Psi}(r_i)$ value and the 68% and 95% (equivalent to the 1σ and 2σ) uncertainty intervals are computed. For all analyses, we will consider a critical level of at least $p = 0.05$ (95%) to declare statistical significance.

>This method was implemented in PYTHON and is available on the project website[22] (Borlaff 2021). In Appendix A, we test this method over a set of eight mock HAWC+ polarization observations using different tilt angles, inclinations, S/Ns, and magnetic pitch angles. Our method allows us to estimate the magnetic pitch angle profile without strong dominating systematic errors at an uncertainty level of $p > 0.05$. Using mock polarization observations with $P/\sigma_p \geqslant 2$, an accuracy of $\leqslant 5°$ is expected in the $\overline{\Psi}(R)$.

Our magnetic pitch angle estimation method entails processing the data on a pixel-by-pixel basis, allowing the user to separate different regions of the galaxy by using masks. Section 4 describes how this masking technique was leveraged to produce measures of the magnetic pitch angle orientation for different regions in M51: (a) full disk, (b) arm versus interarm, and (c) arm 1 versus arm 2.

3.2. Morphological Wavelet Analysis

To compare the magnetic spiral structure with the morphology of the total intensity using several tracers, a measure of the pitch angle of the spiral arms is required. To identify the orientation of the spiral arms in the 154 μm, 3 cm, and 6 cm observations, we take advantage of the technique applied in Patrikeev et al. (2006) and Frick et al. (2016)—the two-dimensional anisotropic wavelet transform—for the identification of elongated structures. Wavelet transforms allow recovery of the PA of the maximum-amplitude wavelet at each pixel where the signal is significant, returning a map of wavelet orientations representing the local pitch angle of the image. The wavelet scale used is 13″8, twice the size of the pixel scale. We refer to the original articles (Patrikeev et al. 2006; Frick et al. 2016, and references therein) for a complete explanation of the method and its mathematical description.

In Section 4.4, we present the wavelet transform maps for the 154 μm FIR, 3 and 6 cm radio intensity images, ^{12}CO(1–0), and 21 cm H I observations. The lines inside the spiral arms closely follow the local structure of the spiral arms for each tracer. Conveniently, the orientation of the wavelet transform can be decomposed into its corresponding Stokes Q and U, allowing analysis of their structure using the same pitch angle method and software described in Section 3.1.

3.3. Morphological Masks

The THINGS 21 cm observations of the H I gas disk (Section 2.3) and the morphological wavelet analysis from Section 3.2 are used to separate the different morphological regions of M51 (spiral arms, interarms, and core). The resulting masks are shown in Figure 4, and the polarization fields separated by the morphological masks for the different wavelengths are shown in Figure 5. We choose the H I gas to define the arm–interarm mask based on two factors: (1) we have high-resolution, deep observations of M51, and more importantly, (2) it allow us to trace the spiral arms closer to the inner core of the galaxy, something that is not possible with lower-resolution data such as those of our FIR observations.

As a first step, the core region is defined by studying the surface brightness profile of the H I disk (see Figure 6). The inner region of the profile ($R < 100″$, <4.16 kpc) shows a nearly constant surface brightness, with a notable decrease of

---

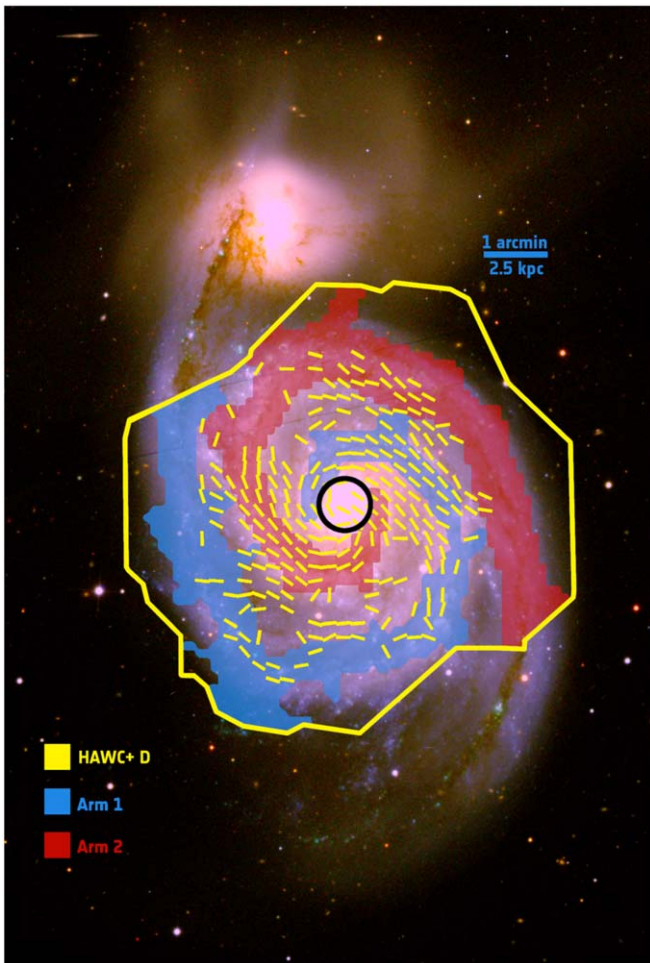[22] SOFIA Legacy Project for Magnetic Fields in Galaxies: http://galmagfields.com/.

Figure 4. General description of the M51 regions for this analysis. In the background is the RGB image based on SDSS *gri* imaging (Gunn et al. 2006). Footprint and *B*-field orientations with their lengths normalized to unity from HAWC+ observations are shown in yellow. Red and blue shaded regions indicate mask and arm definitions; see Section 3.3. The black circle shows the limiting radius of the M51 core region. See the legend for labeling and physical scaling.

the 21 cm emission at $R < 22''$ (<0.9 kpc), corresponding to the core region. We fit the location of the break in the surface brightness profile using the software Elbow[23] (Borlaff et al. 2017), obtaining a break radius of $R_{\text{break}} = 21.2^{+1.8}_{-1.6}{}''$, $0.88^{+0.08}_{-0.07}$ kpc), statistically significant at a level of $p < 10^{-5}$. We define this region as the radial limit for the core region in the morphological mask.

In a second step, the intensity image of the H I observations is analyzed using the wavelet transformation method (see Section 3.2). The amplitude of the wavelet-transformed image provides us with a probability map of the spatial distribution of elongated structures, like spiral arms. We define as statistically significant (and thus part of a spiral arm) every pixel whose associated wavelet amplitude is higher than twice the standard deviation (2σ) of the background noise in the wavelet-transformed image. By doing this, we only select regions that have at least an $\sim$95% probability of being part of an elongated H I structure. Finally, we separate the two spiral arms using a

visually defined polygon over the resulting mask, taking into account the morphology of the galaxy in the FIR, ^{12}CO(1–0), 3 and 6 cm, and H I data sets (see Figure 4).

4. Magnetic Pitch Angle Results

This section describes the results of the magnetic pitch angle profile for different wavelengths (154 μm and 3 and 6 cm) and morphological regions (full disk, arms, and interarms). In order to avoid systematic effects in the results caused by the different spatial resolutions from different data sets, we convolve and rebin the radio observations to the SOFIA/HAWC+ 154 μm resolution (FWHM$_{\text{HAWC+}} = 13''\!.6$). In addition, we use the same location of the polarization measurements in FIR and radio observations, which allows us to study the same LOS at both wavelength regimes. As the FIR observations have a lower S/N than the radio observations, we select statistically significant polarization measurements, $P/\sigma_P \geqslant 2$. The common resolution scale enables the comparison of maps at the same positions, a particularly critical requirement for the analysis of the arm and interarm regions (Sections 4.2 and 4.3).

4.1. Radial Axisymmetric Profile of the Magnetic Pitch Angle: Full Disk

The properties of the magnetic pitch angle across the M51 galactic disk are first analyzed across the full disk mask, with no partition into arm and interarm regions (see Figures 2 and 3). The top panel of Figure 7 shows the radial profiles of the magnetic pitch angles for the full disk after applying the methodology presented in Section 3.1. For the radio polarization observations, we find that the magnetic pitch angle profile is mostly flat up to a radius of $220''$ (9.15 kpc). Similarly, for our FIR observations, the magnetic pitch angle is mostly flat up to a radius of $160''$ (6.66 kpc); for galactocentric radii larger than $R > 160''$ (>6.66 kpc), we find signs of a drop in the magnetic pitch angle profile. The central beam of the observations is shown as a black vertical dashed line in each panel. The pitch angle increases at the center due to resolution effects produced by the small number of polarization measurements available at the core.

For the full disk (Figures 2, 3, and 7), we estimate an average magnetic pitch angle of $\overline{\Psi}^{\text{FD}}_{\text{FIR}} = +23.9^{+1.2}_{-1.2}{}^{\circ}$ for the 154 μm/HAWC+ data set. For the 3 and 6 cm observations, we obtain $\overline{\Psi}^{\text{FD}}_{3\,\text{cm}} = +26.0^{+0.9}_{-0.8}{}^{\circ}$ and $\overline{\Psi}^{\text{FD}}_{6\,\text{cm}} = +28.0^{+0.8}_{-0.6}{}^{\circ}$, which are compatible at some of the bins with the results from Fletcher et al. (2011; see their Table A1). The 3 and 6 cm magnetic pitch angle profiles presented in this work are slightly higher, on average, than those presented in Fletcher et al. (2011) but compatible on the low end in some regions. Specifically, comparing Figure 7 with line 3 of Table A1 in Fletcher et al. (2011), there is reasonable agreement within the error bars in the first three radial ranges. Only in the outer range (6.0–7.2 kpc) does the absolute value of the pitch angle from Fletcher et al. decrease, while it increases in Figure 7. Nevertheless, there is a substantial difference between the two analyses that we must consider. First, their profiles combine polarization observations from 3, 6, 18, and 20 cm data sets, while we are analyzing the 3 and 6 cm wavelengths independently. Second, their pitch angle (p_0) represents the average pitch angle for the dominant of two different large-scale modes of the regular magnetic field, while our profiles represent a nonparametric measurement of the magnetic pitch angle, including variations
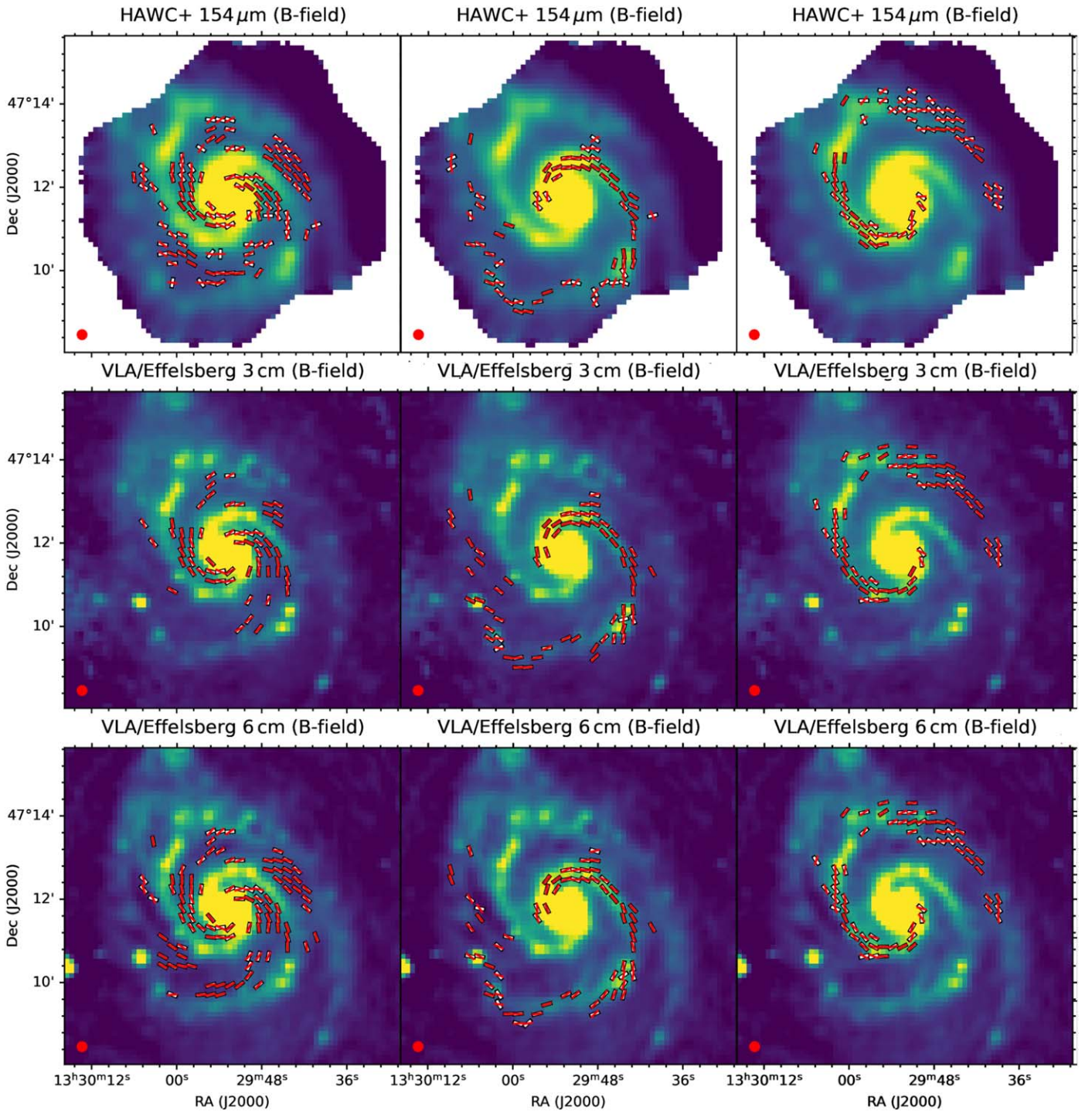
---

[23] Elbow: a statistically robust method to fit and classify the surface brightness profiles. The code is publicly available at GitHub (https://github.com/Borlaff/Elbow).

Figure 5. The *B*-field orientation maps of M51 of 154 μm/HAWC+ (top row) and radio polarimetric observations at 3 cm (middle row) and 6 cm (bottom row; Fletcher et al. 2011) for the interarm (left column), arm 1 (middle column), and arm 2 (right column) morphological regions defined in Section 3.3 (see Figure 4). The white lines represent the measured *B*-field orientations, for which the lengths have been normalized to unity. Red lines show the average polarization orientation estimated from the magnetic pitch angle profile. Total intensity is displayed in the background. See the color bar in Figures 2 and 3 for reference.

on smaller scales. For these reasons, we should consider a direct comparison between both profiles with care.

4.2. Radial Magnetic Pitch Angle Profile: Spiral Arms

Given the angular resolution of the FIR and radio observations, the interarm and arm regions can be separated and analyzed independently. Using the mask described in Section 3.3, we generate three radial profiles of the magnetic pitch angle: arm 1, arm 2, and both spiral arms combined ("Arms region" in Figure 7). We adopt the same notation for the spiral arms of M51 as in Patrikeev et al. (2006; see their Figure 3). From the outskirts of the galaxy, arm 2 is the most northern arm close to M51b, while arm 1 is the most southern arm (Figure 4). We show the polarization measurements used for each region in Figure 5. The results of the magnetic pitch angle profile for both arms combined are shown in the middle panel of Figure 7, labeled as
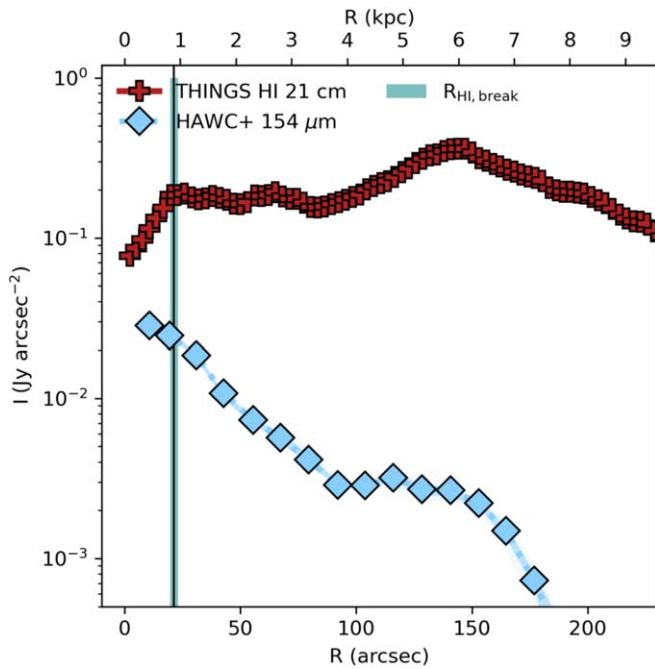
Figure 6. Surface brightness profile analysis of the H I (red plus signs) and FIR (blue diamonds) components of M51. The vertical black solid line and the teal region represent the location of the H I surface brightness break ($R_{\rm break} = 21.2^{+1.8}_{-1.6}{}''$, $0.88^{+0.08}_{-0.07}$ kpc) as estimated using `Elbow` (Borlaff et al. 2017).

"Arms region." Figure 8 shows the magnetic pitch angle profiles for arms 1 and 2 separately at 154 μm, 3 cm, and 6 cm.

For the arms region, we estimate an average magnetic pitch angle of $\overline{\Psi}^{\rm arms}_{\rm FIR} = +16.9^{+1.8}_{-1.7}{}°$ for the 154 μm observations and $\overline{\Psi}^{\rm arms}_{\rm 3\,cm} = +23.1^{+1.1}_{-1.0}{}°$ and $\overline{\Psi}^{\rm arms}_{\rm 6\,cm} = +25.1^{+0.8}_{-0.8}{}°$ for the 3 and 6 cm observations, respectively. The magnetic pitch angle profiles of the spiral arms reveal an interesting scenario. The radio polarization maps at 3 and 6 cm trace a relatively flat pitch angle up to a radius of 220″ (9.15 kpc), showing some steady increase with radius. The FIR magnetic pitch angle suffers a strong break at a radius of ~150″ (~6.24 kpc), decreasing suddenly toward negative values. Statistical analysis of the probability distributions obtained with the Monte Carlo simulations of each bin beyond the ~150″ break reveals that the difference is significant ($p < 0.05$) and consistent up to the limiting radius of observation on M51.

The observed break in the magnetic pitch angle profile of the arms region has a significant impact on the average value. In Figure 9, we compare the global differences in the magnetic pitch angle between FIR and radio wavelengths. We measure the difference in average magnetic pitch angle for each pair of data sets (154 μm, 3 cm, and 6 cm) and arms regions of M51. The vertical histograms in Figure 9 represent the probability distribution for the difference in the median pitch angle as a function of the wavelengths and regions compared. These probability distributions are generated based on the 10,000 Monte Carlo simulations obtained for the magnetic pitch angle analysis. The distributions take into account the uncertainties in PA, inclination, and Stokes IQU from the different sets of polarization maps. Using these simulations, we are able to reconstruct the realistic probability density distribution of the average difference between the magnetic pitch angle profiles. We find a statistically significant difference in the magnetic

pitch angle between FIR and radio wavelengths in the arms. Averaged across the complete extension of both arms, the FIR magnetic pitch angle is $-6.2^{+2.1}_{-2.0}{}°$ and $-8.3^{+2.0}_{-1.9}{}°$ lower than that measured in 3 and 6 cm, a result significant with p-values of 0.002 and $<10^{-4}$, respectively.

We now analyze the two arms separately in Figure 8. Results show that the two arms have different radial profiles of the magnetic pitch angles across the galactocentric radius. At small radii ($R < 75''$, >3.12 kpc), arm 1 shows a lower magnetic pitch angle than arm 2, $\overline{\Psi}^{A1} < \overline{\Psi}^{A2}$. The magnetic pitch angle profile is inverted at $R > 75''$ (>3.12 kpc), where $\overline{\Psi}^{A1} > \overline{\Psi}^{A2}$. This inversion is observed at all wavelengths up to $R \sim 160''$ (6.66 kpc). At $R > 160''$ (>6.66 kpc), the magnetic pitch angle of both arms shows a sharp decrease toward zero and negative values in FIR but not in the 3 and 6 cm radio polarization observations. For the 3 and 6 cm radial profiles, the magnetic pitch angle of arm 1 is mostly flat beyond $R > 75''$ (>3.12 kpc), while arm 2 presents an upturn at $R > 150''$ (>6.24 kpc). A high pitch angle dispersion region is found in arm 1 at $R \sim 150''$ (~ 6.24 kpc) on the 154 μm/HAWC+ magnetic pitch angle profile.

We further explore the pitch angle difference for FIR and radio polarization observations in the northern section of arm 2, one of the closest—but not physically connected—spiral arm regions to M51b. We study the distribution of magnetic pitch angles in a rectangular aperture of 3.45×2.07 arcmin^2 (8.6×5.2 kpc^2) centered at $\alpha = 202°.47$, $\delta = 47°.23$. Figure 10 shows the B-field orientations for the 154 μm, 3 cm, and 6 cm observations. Visual inspection of the three B-fields shows that, on average, the magnetic field at 154 μm shows a different orientation with a smaller pitch angle than those from radio polarimetric observations. In the left panel, we show the probability distributions for the average value of the pitch angle in that aperture. The results show a systematic difference ($p < 10^{-4}$) between the FIR and the two radio observations. The magnetic pitch angles of 3 and 6 cm are compatible with each other. The average magnetic pitch angles in this region are $\overline{\Psi}_{\rm FIR} = -8.5^{+2.8}_{-2.7}{}°$, $\overline{\Psi}_{\rm 3\,cm} = +7.8^{+1.8}_{-1.8}{}°$, and $\overline{\Psi}_{\rm 6\,cm} = +7.2^{+1.4}_{-1.3}{}°$.

We repeat the analysis on an equivalent aperture located in the southern region of arm 1, symmetrically separated from the core ($\alpha = 202°.46$, $\delta = 47°.16$, also with an area of 8.6×5.2 kpc^2). The results show that the average magnetic pitch angle in this region is $\overline{\Psi}_{\rm FIR} = +5.8^{+5.2}_{-5.3}{}°$, which is significantly ($p < 10^{-4}$) lower than those measured in 3 ($\overline{\Psi}_{\rm 3\,cm} = +29.1^{+2.8}_{-2.6}{}°$) and 6 ($\overline{\Psi}_{\rm 6\,cm} = +28.3^{+1.2}_{-1.5}{}°$) cm. These results—including the magnetic pitch angle profiles—confirm that the magnetic field in the outskirts of M51 traced by radio and FIR polarization observations is different.

Our results show that the structure of the magnetic field is not isotropic or homogeneous across the galactic disk. Interestingly, the independent trends of the two spiral arms in the inner region of the disk ($R < 150''$, <6.24 kpc) are detected in the three wavelengths independently, ensuring that the quality of the observations and the analysis are high enough to confirm that the radial changes in magnetic pitch angle are not caused by statistical uncertainty. In addition, we find that this feature is systematically present in both spiral arms at FIR wavelengths, confirming that the change in magnetic pitch angle is a detectable feature of the magnetic spiral structure of M51.
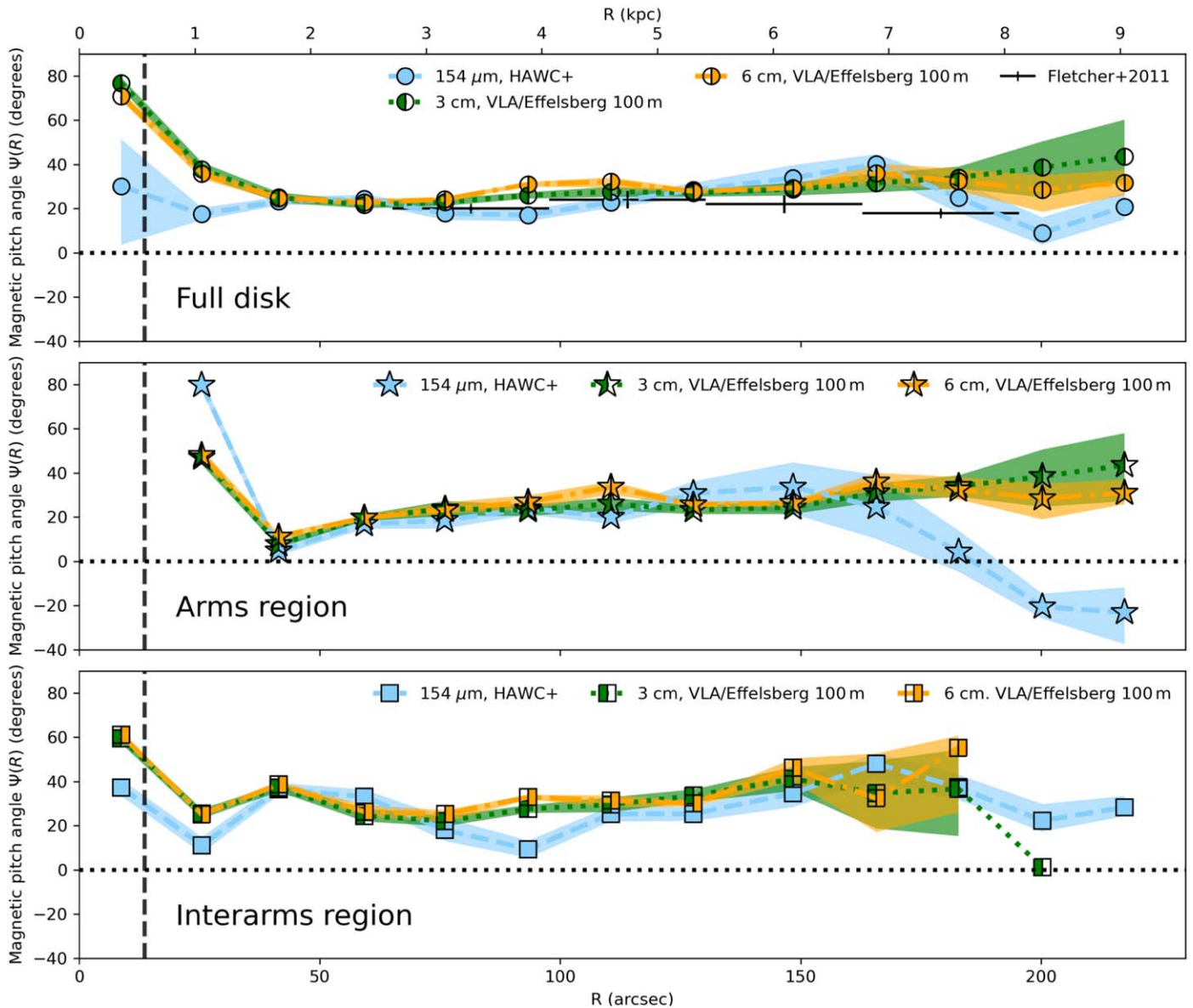
Figure 7. Magnetic pitch angle profiles for the FIR 154 μm HAWC+ observations (this work) and the 3 and 6 cm radio polarimetric observations (Fletcher et al. 2011) of M51. On the vertical axis, we represent the average magnetic pitch angle profile $\Psi(R)$ per radial bin as a function of radius. Top panel: profile for the full disk region, assuming axisymmetry and homogeneity. Middle panel: arm region profile. Bottom panel: interarm region profile. See the legend for the colors and line types. The central beam of the observations is shown as a black vertical dashed line in each figure.

4.3. Radial Magnetic Pitch Angle Profile: Interarms

We analyze the interarm region in Figure 7, whose polarization measurements and models are shown in Figure 5. At all wavelengths, the interarm magnetic pitch angle shows a fairly constant structure up to 220″ (9.15 kpc). We estimate the average magnetic pitch angles to be $\overline{\Psi}_{FIR}^{IA} = +28.6_{-1.3}^{+1.3\circ}$, $\overline{\Psi}_{3\,cm}^{IA} = +29.1_{-1.0}^{+1.0\circ}$, and $\overline{\Psi}_{6\,cm}^{IA} = +30.6_{-0.8}^{+1.0\circ}$ for the 154 μm, 3 cm, and 6 cm observations, respectively. The magnetic pitch profiles and their average values show that the interarm magnetic field structure of M51 is the same at FIR and radio wavelengths. However, we find that the interarm magnetic pitch angles are higher than the corresponding values for the arm regions (Section 4.2). This is significant at a p-value $<10^{-4}$ for 154 μm, 3 cm, and 6 cm.

The most striking result from the comparison of the interarm magnetic pitch angle profiles is that the 154 μm observations do not show signs of the same distortions or radial variations as those detected in the spiral arms (Section 4.2 and Figure 5). The interarm radial profile appears to be relatively smooth and constant across the galaxy disk up to the observed outer radius of 220″ (9.15 kpc). In Figure 9 (bottom row), we compare the global differences in the magnetic pitch angle between FIR and radio wavelengths, this time for the interarm region. We do not find any significant difference between the average magnetic pitch angle value of the FIR and radio polarization data sets in the interarm region, confirming the results from the previous profiles.

A summary of the average magnetic pitch angles within the radial range of 21″2–220″ (0.88–9.15 kpc) is shown in Table 2.
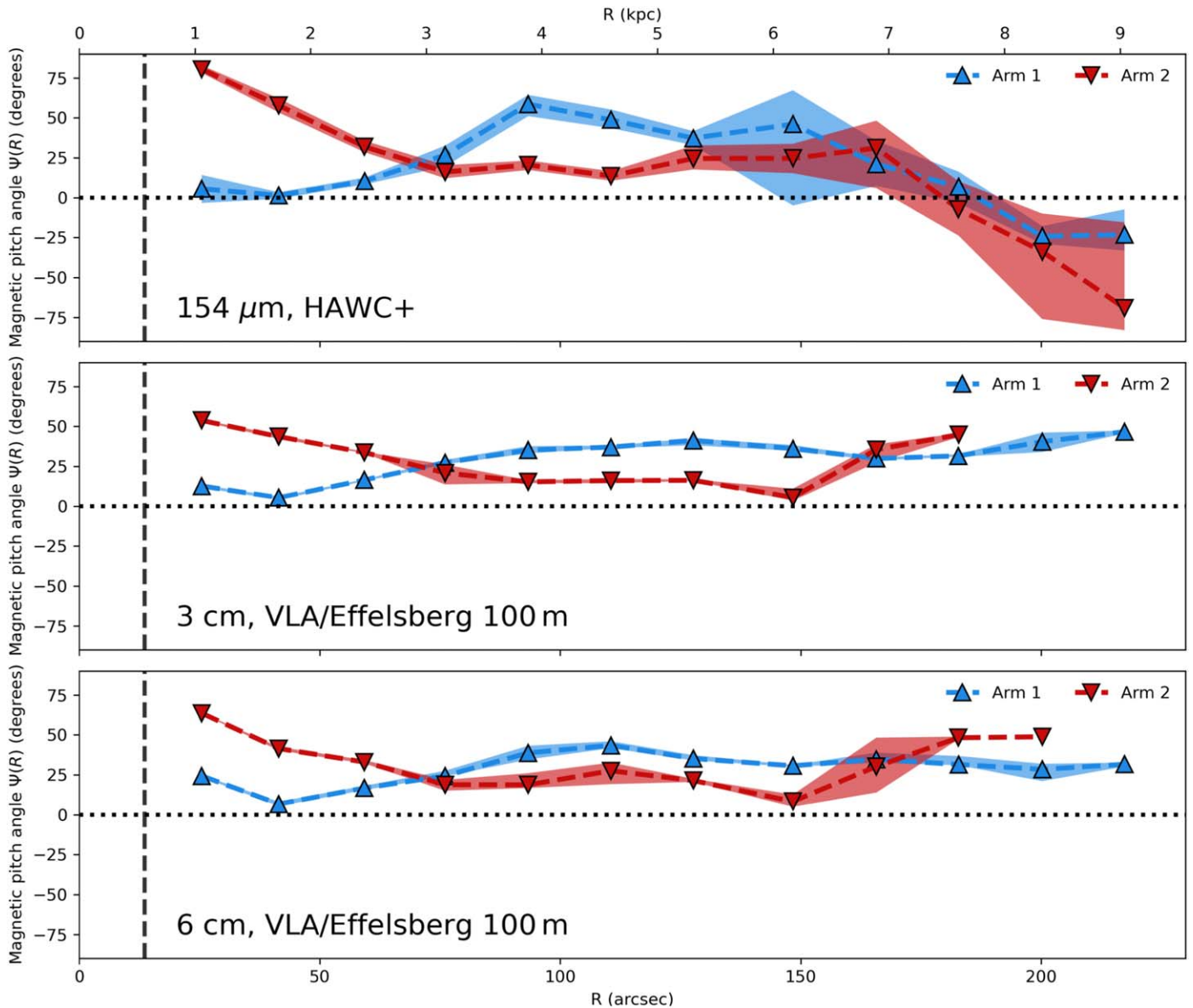
Figure 8. Magnetic pitch angle profiles for the spiral arm 1 (blue) and arm 2 (red) of M51 as a function of wavelength. In each panel, we present the average magnetic pitch angle profile $\Psi(R)$ per radial bin as a function of radius. Top panel: profile for the 154 μm/HAWC+ observations. Middle panel: magnetic pitch angle profile for 3 cm. Bottom panel: magnetic pitch angle profile for 6 cm. See the legend for the colors and line types.

Based on the results from previous sections, we conclude the following.

1. The outer ($R > 6.24$ kpc) magnetic spiral structure of the spiral arms in M51 is wrapped tighter when measured in FIR than in radio wavelengths.
2. The FIR interarm magnetic pitch angle structure is similar to that traced with the radio polarization observations in the diffuse ISM.

These results suggest that the outer field decoupling of the FIR and radio magnetic fields is only associated with the spiral arms. This result is further confirmed with the observations of the magnetic pitch angle profiles and custom apertures studied in Section 4.2. We note that this difference is significant, despite the fact that the radial binning and the combination in azimuthal coordinates may be smoothing the differences found

in the histograms from this section. We discuss the implications of these results in Section 6.

4.4. Comparison with the Morphological Pitch Angle of the Spiral Arms

Figures 11 and 12 show the morphological pitch angle maps of the 154 μm, 3 cm, 6 cm, ^{12}CO(1–0), and 21 cm H I observations. These maps have been constructed from the total intensity images and wavelet transform method described in Sections 3.1–3.2. To avoid selection effects due to the different resolution of the images, we convolved every data set to the 154 μm HAWC+ beam size, as we did in the previous section for the VLA/Effelsberg 100 m observations. In Figure 13, we present the morphological pitch angle profiles of the spiral arms for the five different data sets considered, plus the comparison
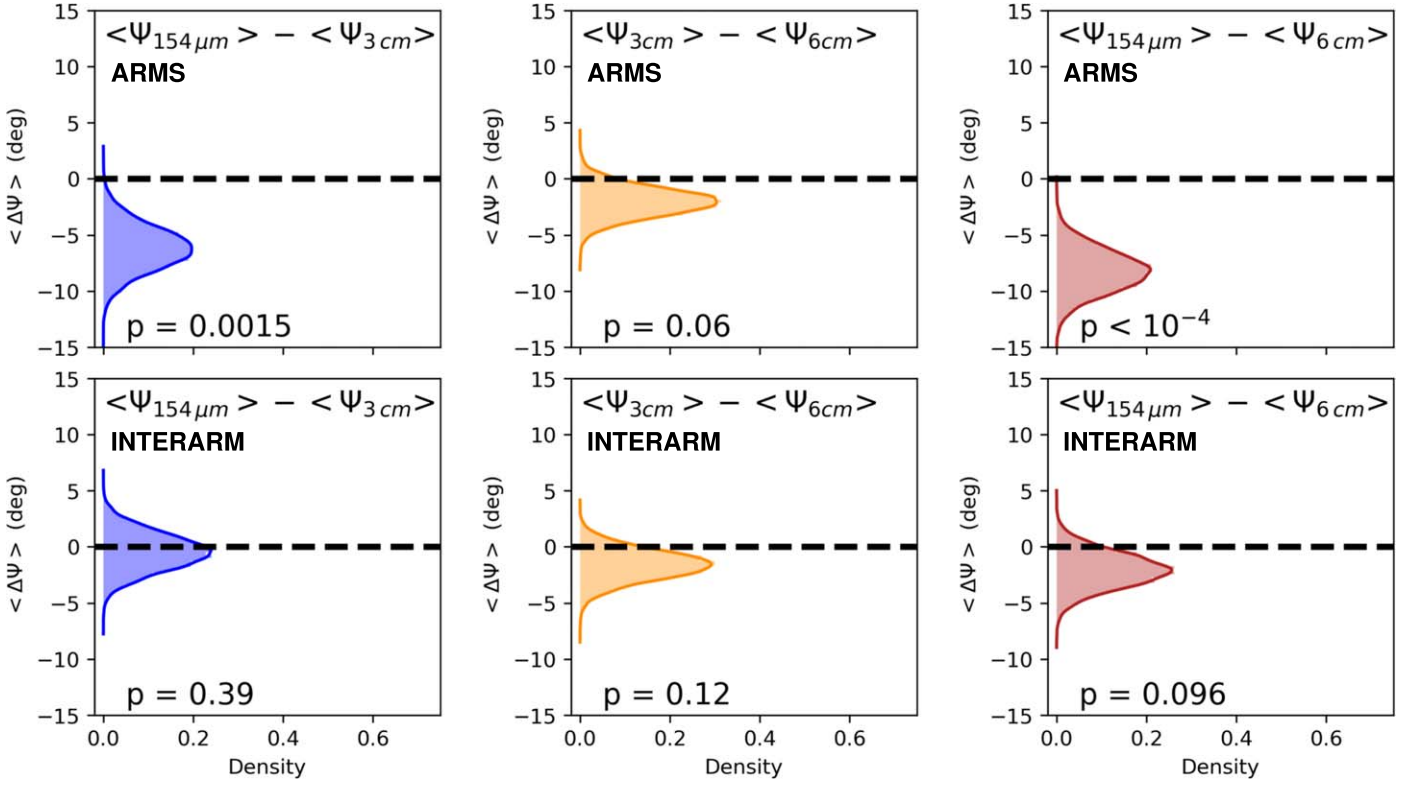
Figure 9. Probability density distributions of the difference in median magnetic pitch angle ($\langle\Delta\Psi\rangle$, vertical histograms). Columns from left to right: 154 μm vs. 3 cm, 3 cm vs. 6 cm, and 154 μm vs. 6 cm. Rows from top to bottom: arm region (arm 1 + arm 2) and interarm region. The horizontal black dashed line represents the zero level (no difference). The p-value in each panel represents the probability that the distribution is compatible with zero (no difference).

of the magnetic and morphological pitch angle for 154 μm, 3 cm, and 6 cm.

The morphological pitch angles of 154 μm, 3 cm, and 6 cm have a similar radial profile, i.e., $\overline{\Psi}_{\rm FIR}^{\rm morph} \sim \overline{\Psi}_{3\,\rm cm}^{\rm morph} \sim \overline{\Psi}_{6\,\rm cm}^{\rm morph}$. At low radii ($<120''$, <5.0 kpc), the morphological pitch angle is relatively high, starting at $\sim 60°$–$70°$. At higher radii ($>120''$, <5.0 kpc), the morphological pitch angle decreases to $0°$–$10°$ with a relatively slow increase showing some scatter in the outskirts ($>200''$, 8.32 kpc), especially for 154 μm. We also compare the distribution of the morphological pitch angle with the magnetic pitch angle profiles obtained in Sections 4.1–4.3 (see the third, fourth, and fifth panels of Figure 13). The analysis shows that for the three bands analyzed, the magnetic pitch angle is lower than the morphological equivalent up to a radius of $\sim 100''$ (~ 4.16 kpc). At larger radii ($>100''$, >4.16 kpc), the magnetic pitch angle is larger than the morphological pitch angle. The exception is in the outermost region ($>175''$, >7.28 kpc) of the 154 μm/HAWC+ data due to the magnetic pitch angle break reported in Section 4.2.

For ^{12}CO(1–0), we find a relatively constant, albeit with large scatter, pitch angle profile of $\overline{\Psi}_{\rm CO}^{\rm Morph} \sim 40°$–$60°$ up to the limit of the PAWS observations ($R = 120''$, ~ 5 kpc), with an average of $\overline{\Psi}_{\rm CO}^{\rm Morph} = 30.7^{+0.5°}_{-0.4}$. For the 21 cm H I observations, we find a relatively constant morphological pitch angle of $\overline{\Psi}_{21\,\rm cm}^{\rm Morph} = 9.9^{+0.3°}_{-0.5}$ across the whole observable disk. We find that the morphological pitch angle of H I is smaller than at FIR, radio, and ^{12}CO(1–0) within the central 120$''$ (5 kpc). But it is approximately similar to that of the outer region ($R > 120''$, >5 kpc) when compared with the 154 μm ($\overline{\Psi}_{\rm FIR}^{\rm Morph} = 8.4^{+0.5°}_{-0.5}$), 3 cm ($\overline{\Psi}_{3\,\rm cm}^{\rm Morph} = 10.6^{+0.7°}_{-0.9}$), and 6 cm ($\overline{\Psi}_{6\,\rm cm}^{\rm Morph} = 13.0^{+0.7°}_{-0.6}$). For reference, the average magnetic pitch angles in the outer region

of the spiral arms are $\overline{\Psi}_{\rm FIR}^{\rm Arms} = 15.2^{+4.0°}_{-4.2}$, $\overline{\Psi}_{3\,\rm cm}^{\rm Arms} = 25.9^{+1.5°}_{-1.5}$, and $\overline{\Psi}_{6\,\rm cm}^{\rm Arms} = 27.5^{+1.1°}_{-1.1}$.

We find that the magnetic field pitch angles are higher than the morphological pitch angles of the H I in the outskirts of the spiral arms of M51. The p-value for this difference in average values is lower than 10^{-4} for the 3 and 6 cm observations (highly significant) and $p = 0.044$ for the 154 μm observations. The higher values for the outermost bins of the FIR morphological pitch angle profile are possibly an artifact caused by the boundaries of the HAWC+ footprint with the wavelet algorithm; thus, we consider them negligible. In addition, the lower significance at 154 μm is caused by the observed magnetic pitch angle break in the outskirts, which, combined with the outer distortions on the morphological profile, reduces the difference between the morphological and magnetic values.

Close inspection of the total intensity distribution in Figures 11 and 12 reveals that the 154 μm, 3 cm, 6 cm, and ^{12}CO(1–0) data sets show bright emission in the core of M51. Contrarily, 21 cm H I observations show no detectable emission at small radii, as previously mentioned in Section 3.3. These different distributions can be responsible for the difference in the morphological pitch angle distributions at inner radii ($<120''$, <5 kpc). The main reason is that the direction of the wavelet field is affected by the presence of a large, bright, radial central gradient from the core. Nevertheless, the facts that (1) we observe this relatively higher pitch angle value up to $R \sim 100''$ (4.16 kpc), far away from the main component of the total intensity of the core, and (2) the ^{12}CO(1–0) data set also shows a higher morphological pitch angle than the H I observations suggest that the morphological differences of the
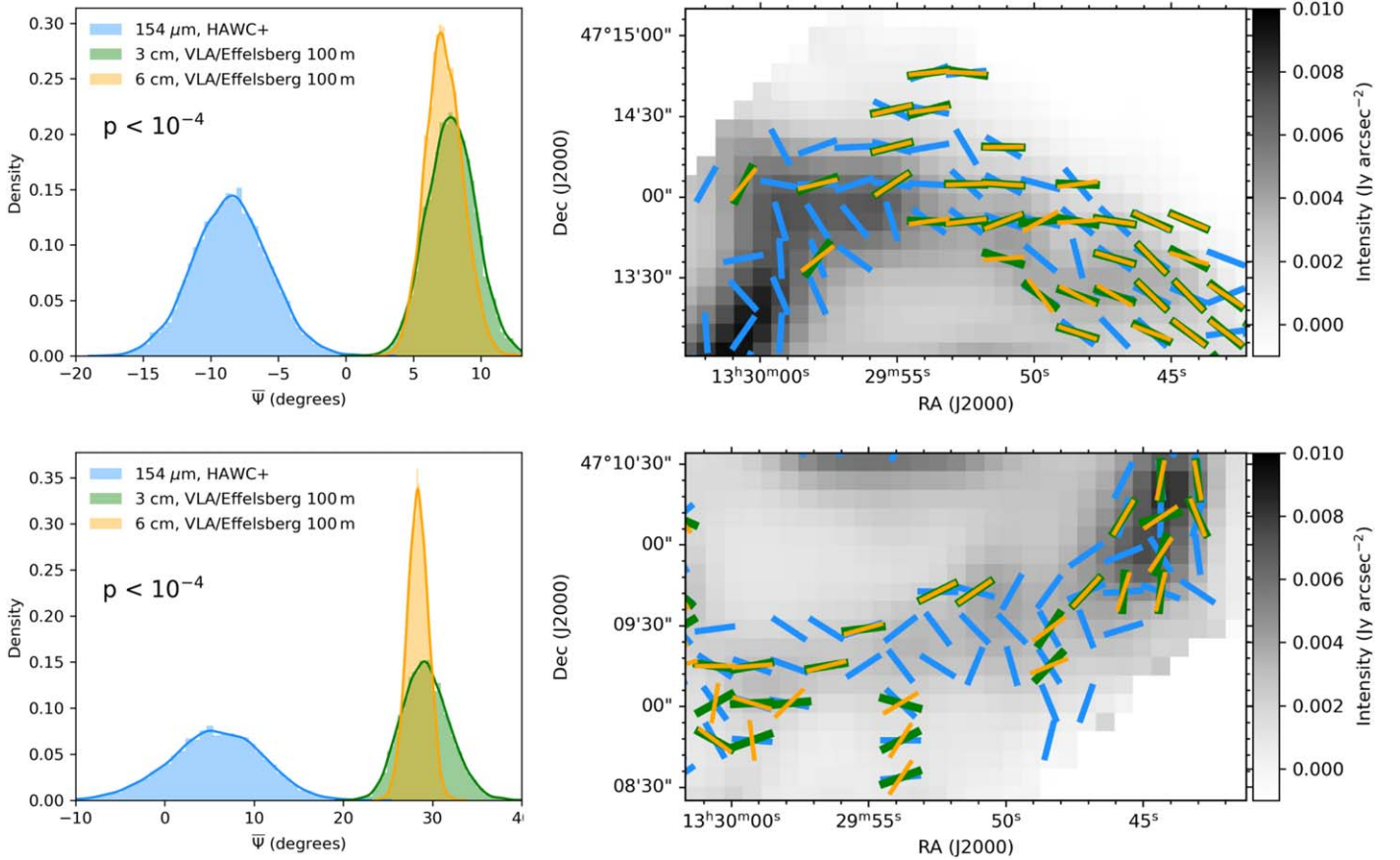
Figure 10. Analysis of the magnetic pitch angle difference in the northern (top row) and southern (bottom row) region of the M51 spiral arms. Left panel: probability distribution of the median magnetic pitch angle for the 154 μm, 3 cm, and 6 cm observations. Right panel: B-field orientations for 154 μm, 3 cm, and 6 cm. The gray-scale background image shows the FIR total intensity from Figure 2. For better visualization, only one of every two polarization measurements is represented. See the color legend in the left panel for reference.

Table 2
Magnetic Field Pitch Angles in the Radial Range of $21\rlap{.}{''}2$–$220''$ (0.88–9.15 kpc) from Figure 7

Wavelength	Full Disk (Ψ^{FD}, deg)	Arm Region (Ψ^{Arms}, deg)	Interarm Region (Ψ^{IA}, deg)
154 μm	$23.9^{+1.2}_{-1.2}$	$16.9^{+1.8}_{-1.7}$	$28.6^{+1.3}_{-1.3}$
3 cm	$26.0^{+0.9}_{-0.8}$	$23.1^{+1.1}_{-1.0}$	$29.1^{+1.0}_{-1.0}$
6 cm	$28.0^{+0.8}_{-0.6}$	$25.1^{+0.8}_{-0.8}$	$30.6^{+1.0}_{-0.8}$

pitch angles for the spiral arms are not caused entirely by systematic effects from the central zone.

In summary, we find the following for the spiral arms.

1. The morphological pitch angles change as a function of the multiphase ISM, such as $\overline{\Psi}^{\mathrm{Morph}}_{\mathrm{H\,I}} < \overline{\Psi}^{\mathrm{Morph}}_{\mathrm{CO}} < \overline{\Psi}^{\mathrm{Morph}}_{\mathrm{FIR}} \sim \overline{\Psi}^{\mathrm{Morph}}_{\mathrm{3\,cm}} \sim \overline{\Psi}^{\mathrm{Morph}}_{\mathrm{6\,cm}}$.
2. The morphological pitch angles at FIR and radio wavelengths are similar across the full disk of M51.
3. At FIR and radio and within the inner $100''$ (4.16 kpc), the magnetic pitch angles are wrapped tighter than the morphological pitch angles.
4. At FIR and radio and at a radius $>100''$ (>4.16 kpc), the magnetic pitch angles of the spiral arms are larger than those from the morphological structure. The exception is the FIR, whose magnetic pitch angle becomes tighter than the morphological pitch angle at a radius $>200''$ (>8.32 kpc).

5. Magnetic Fields in the Multiphase ISM

5.1. The Multiphase ISM

To analyze how the different physical regimes of the multiphase ISM affect the B-fields in M51, we use the velocity dispersion of the neutral and molecular gas as a proxy for the kinetic energy of the turbulence in the ISM. We also use the column density of the galactic disk to study the effect of extinction as a function of the FIR and radio polarization.

In Figure 14, we analyze the variation of the total intensity (I), polarized intensity (PI), and polarization fraction (P) at 154 μm and radio wavelengths as functions of the column density ($N_{\mathrm{H\,I+2H_2}}$). All ρ correlation coefficients in the figures are based on the Spearman nonparametric test. The distributions of the interarm, arm 1, and arm 2 regions are shown in the diagrams. We selected FIR polarization measurements with $\mathrm{PI}/\sigma_{\mathrm{PI}} \geqslant 3$, $\sigma_{\mathrm{P}} \leqslant 15\%$, and $P \leqslant 30\%$. For the selected measurements, the minimum S/N in polarization fraction equals 3. Note that we selected the cut in polarized flux such that it reduced any effects due to the positive bias of the polarization fraction. The medians of the physical parameters of the arm 1, arm 2, and interarm zones studied in this section are shown in Table 3. For simplicity, here we only show the diagrams in 3 cm, but the same results are obtained in 6 cm data sets (see Table 3 and the 6 cm radio polarization diagrams in Appendix C).

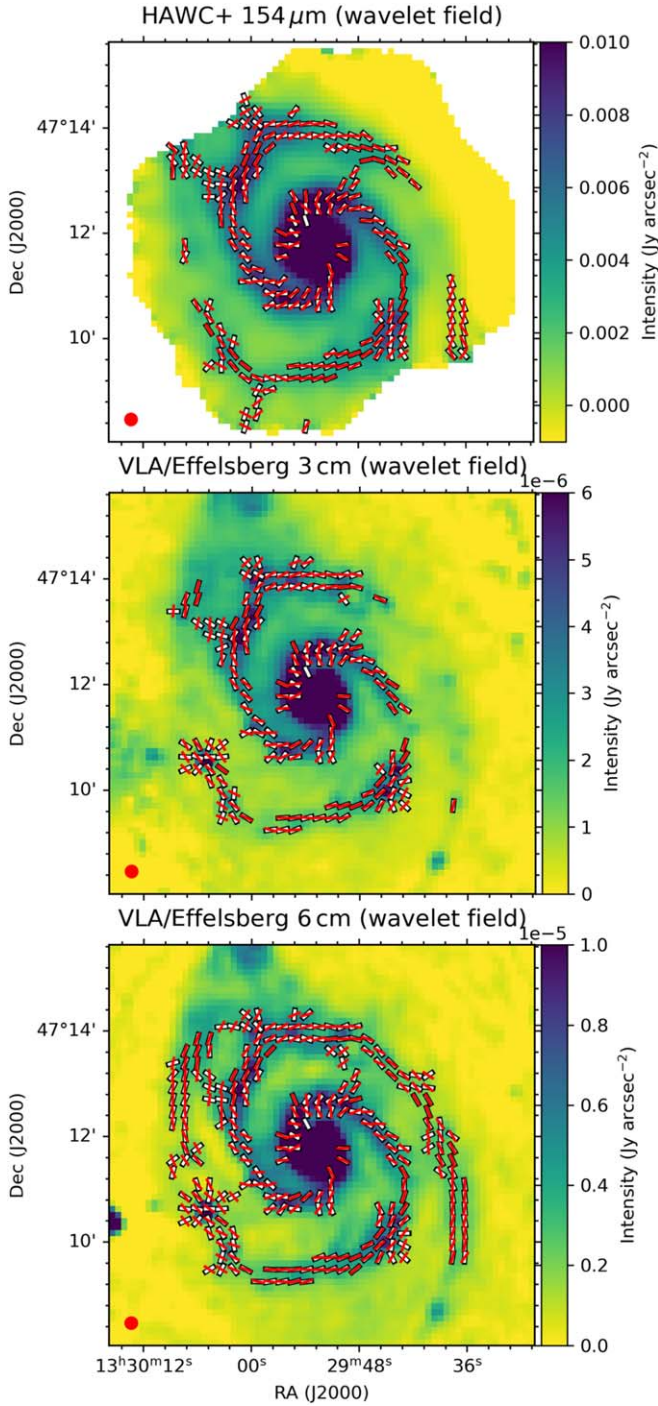At 154 μm, we find a strong positive linear correlation between the total intensity and the column density

Figure 11. Top to bottom: surface brightness distributions for HAWC+ 154 μm, VLA/Effelsberg 3 cm, and VLA/Effelsberg 6 cm, with the morphological wavelet line plotted in red. In white, we show the azimuthally averaged morphological pitch angle directions. The red circle shows the resolution element (beam size) of the analyzed maps.
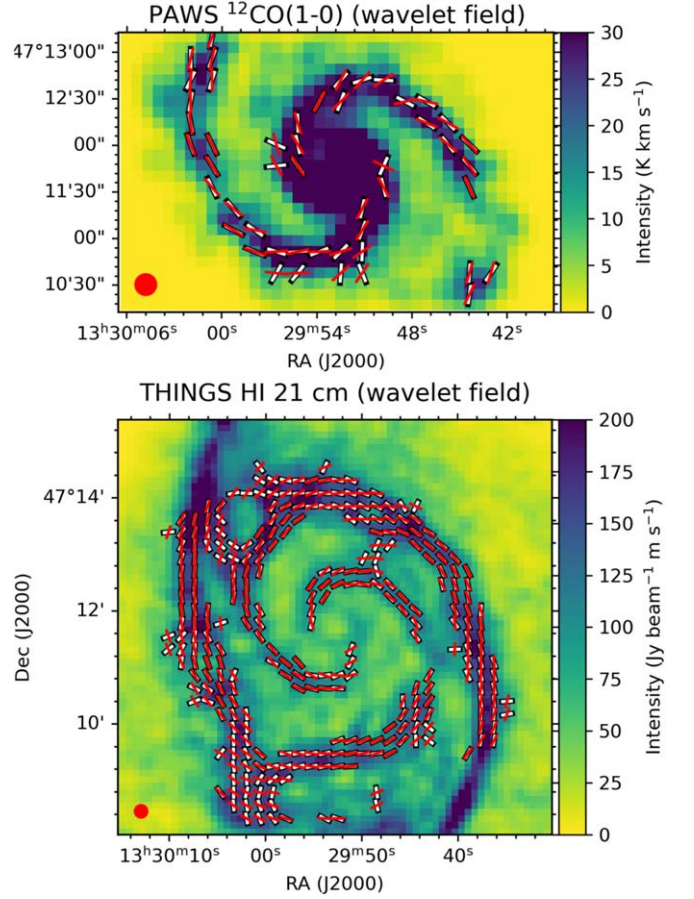

Figure 12. Top to bottom: surface brightness distributions for ^{12}CO(1–0) PAWS and THINGS H I observations with the morphological wavelet line overplotted (red). In white, we show the averaged morphological pitch angle profile. The red circle shows the resolution element (beam size) of the analyzed maps.

$N_H/A_V = (2.21 \pm 0.09) \times 10^{21}$ cm^{-2} mag^{-1} (Güver & Özel 2009), the change in slope corresponds to an extinction of $A_V = 1.40^{+0.18}_{-0.12}$ mag.

At radio wavelengths, the total intensity increases with the column density, with a slope of the $\log_{10}(I)$ versus $\log_{10}(N_{H\,I+2H_2}[$ cm $^{-2}])$ relation of 1.16 ± 0.03. The radio polarization fraction is fairly constant within the full range of column densities, while the polarized intensity increases with increasing column density ($\rho > 0.5$, $p < 0.05$ in all components). For both FIR and radio, we find no strong systematic differences in the trends and distributions of the arm 1, arm 2, and interarm zones in any case (see ρ correlation coefficients in Figure 14).

In Figure 15, we show the analysis as a function of the ^{12}CO(1–0) velocity dispersion ($\sigma_{v,^{12}CO(1-0)}$). In the FIR, the total intensity increases with increasing the velocity dispersion of the molecular gas, the polarization fraction decreases with increasing the velocity dispersion of the molecular gas ($p < 0.05$ in all components), and the polarized intensity remains fairly constant ($\rho < 0.3$, not significant in arm 2). The interarm region has a lower dispersion velocity ($p = 4.8 \times 10^{-22}$, using the nonparametric two-sample comparison Anderson–Darling test; Scholz & Stephens 1987) than arms 1 and 2, dominating at $\sigma_{v,^{12}CO(1-0)} \sim$ 3–5 km s^{-1}. Arm 2 presents a more extended $\sigma_{v,^{12}CO(1-0)}$ distribution than arm 1, reaching values as high as 10 km s^{-1}. Both arms present a 1.0% probability of having the same ^{12}CO(1–0) velocity dispersion.

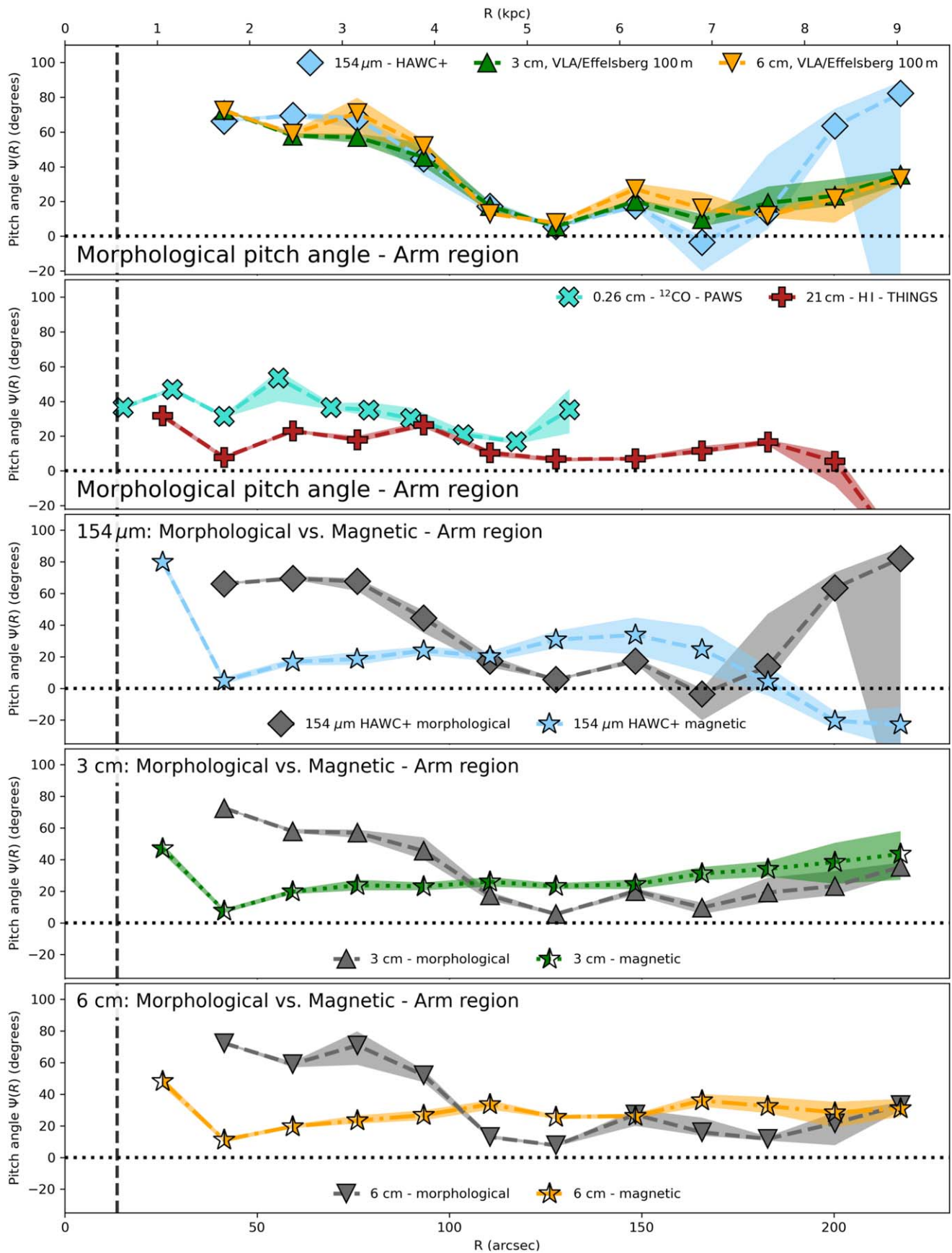$N_{H\,I+2H_2}$. The polarization fraction decreases with increasing column density, while the polarized intensity remains fairly constant across the full range of column densities, i.e., $\log_{10}(N_{H\,I+2H_2}[cm^{-2}]) = [21.0–22.1]$. The FIR polarization fraction is found to change in slope at $\log_{10}(N_{H\,I+2H_2}[cm^{-2}]) = 21.49^{+0.03}_{-0.02}$ (we follow the same method used in Section 3.3 to measure the H I break). Using the relation between the optical extinction, A_V, and hydrogen column density, N_H, relation,

Figure 13. Morphological pitch angle profiles (pitch angle $\Psi(R)$ as a function of the galactocentric radius, R). Top to bottom: 154 μm, 3 cm, and 6 cm; ^{12}CO(1–0) and 21 cm; 154 μm morphological vs. magnetic profile; 3 cm morphological vs. magnetic; and 6 cm morphological vs. magnetic. The profiles are calculated on the arm region of M51. See the legend for the colors and line types.
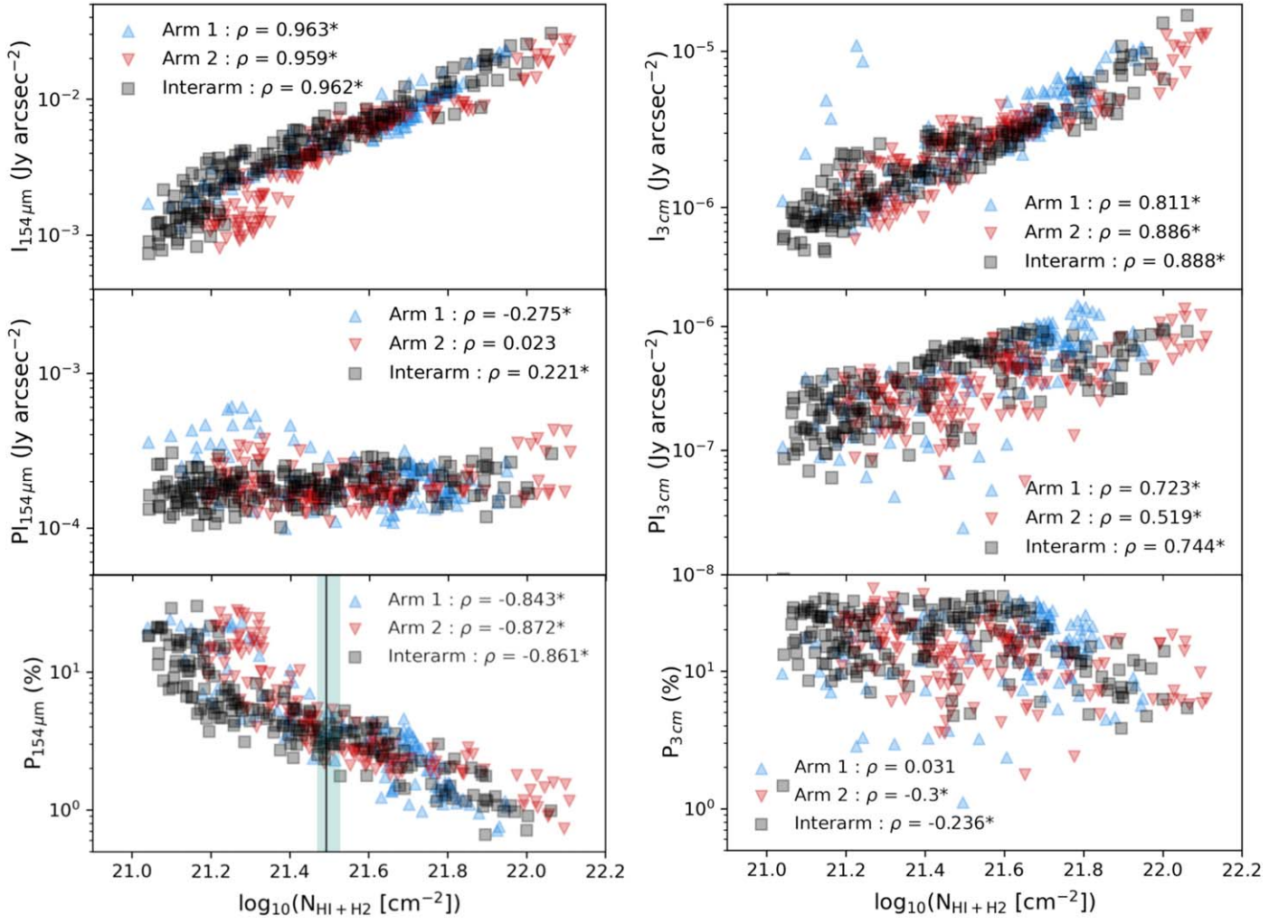
Figure 14. Comparison between 154 μm (left column) and 3 cm (right column) of the total intensity (top row), polarized intensity (middle row), and polarization fraction (bottom row) as a function of gas column density ($N_{\rm HI+2H_2}$). Arm 1 (blue upward-pointing triangles), arm 2 (red downward-pointing triangles), and interarm (black squares) are as defined in Figure 5. See the legend in each panel for the correlation analysis. An asterisk is shown following the ρ correlation coefficient if the correlation is statistically different from zero ($p < 0.05$). The change in slope at $\log_{10}(N_{\rm HI+2H_2}) \sim 21.49$ is shown as a black solid line and 1σ dashed area in the $P_{154\mu m}$–$N_{\rm HI+2H_2}$ plots.

Table 3
Medians of the Physical Parameters of the Arm 1, Arm 2, and Interarm Zones

	Parameter	Wavelength	Arm 1	Arm 2	Interarm
(1)	I (Jy arcsec^{-2})	154 μm	$6.58^{+0.54}_{-0.36} \times 10^{-3}$	$5.10^{+0.56}_{-0.11} \times 10^{-3}$	$4.08^{+0.48}_{-0.26} \times 10^{-3}$
(2)		3 cm	$3.48^{+0.26}_{-0.27} \times 10^{-6}$	$2.60^{+0.16}_{-0.16} \times 10^{-6}$	$1.88^{+0.17}_{-0.15} \times 10^{-6}$
(3)		6 cm	$6.58^{+0.30}_{-0.37} \times 10^{-6}$	$4.68^{+0.35}_{-0.31} \times 10^{-6}$	$3.30^{+0.26}_{-0.19} \times 10^{-6}$
(4)	PI (Jy arcsec^{-2})	154 μm	$2.04^{+0.15}_{-0.11} \times 10^{-4}$	$1.79^{+0.08}_{-0.08} \times 10^{-4}$	$1.86^{+0.08}_{-0.08} \times 10^{-4}$
(5)		3 cm	$5.41^{+0.62}_{-0.50} \times 10^{-7}$	$3.29^{+0.26}_{-0.26} \times 10^{-7}$	$3.43^{+0.18}_{-0.39} \times 10^{-7}$
(6)		6 cm	$9.80^{+0.80}_{-0.67} \times 10^{-7}$	$6.73^{+0.35}_{-0.34} \times 10^{-7}$	$7.58^{+0.63}_{-0.47} \times 10^{-7}$
(7)	P (%)	154 μm	$3.0^{+0.3}_{-0.3}$	$3.5^{+0.4}_{-0.3}$	$4.2^{+0.3}_{-0.3}$
(8)		3 cm	$15.9^{+1.5}_{-1.5}$	$13.5^{+1.0}_{-1.1}$	$17.9^{+1.2}_{-1.1}$
(9)		6 cm	$16.2^{+1.4}_{-1.3}$	$14.7^{+1.0}_{-1.0}$	$22.9^{+1.2}_{-1.3}$
(10)	$\log_{10}(N_{\rm HI+2H_2})[{\rm cm}^{-2}]$		$21.66^{+0.01}_{-0.02}$	$21.49^{+0.04}_{-0.02}$	$21.40^{+0.02}_{-0.03}$
(11)	$\sigma_{^{12}{\rm CO}(1-0)}$ (km s^{-1})		$5.77^{+0.13}_{-0.08}$	$5.61^{+0.15}_{-0.22}$	$4.29^{+0.09}_{-0.07}$
(12)	$\sigma_{\rm HI}$ (km s^{-1})		$18.22^{+0.35}_{-0.20}$	$21.34^{+0.32}_{-0.30}$	$23.40^{+0.34}_{-0.21}$

Note. Rows from top to bottom: (1)–(3) total intensity for 154 μm, 3 cm, and 6 cm; (4)–(6) polarized intensity for 154 μm, 3 cm, and 6 cm; (7)–(9) polarization fraction for 154 μm, 3 cm, and 6 cm; (10) H I column density; (11) ^{12}CO(1–0) velocity dispersion; (12) H I velocity dispersion.

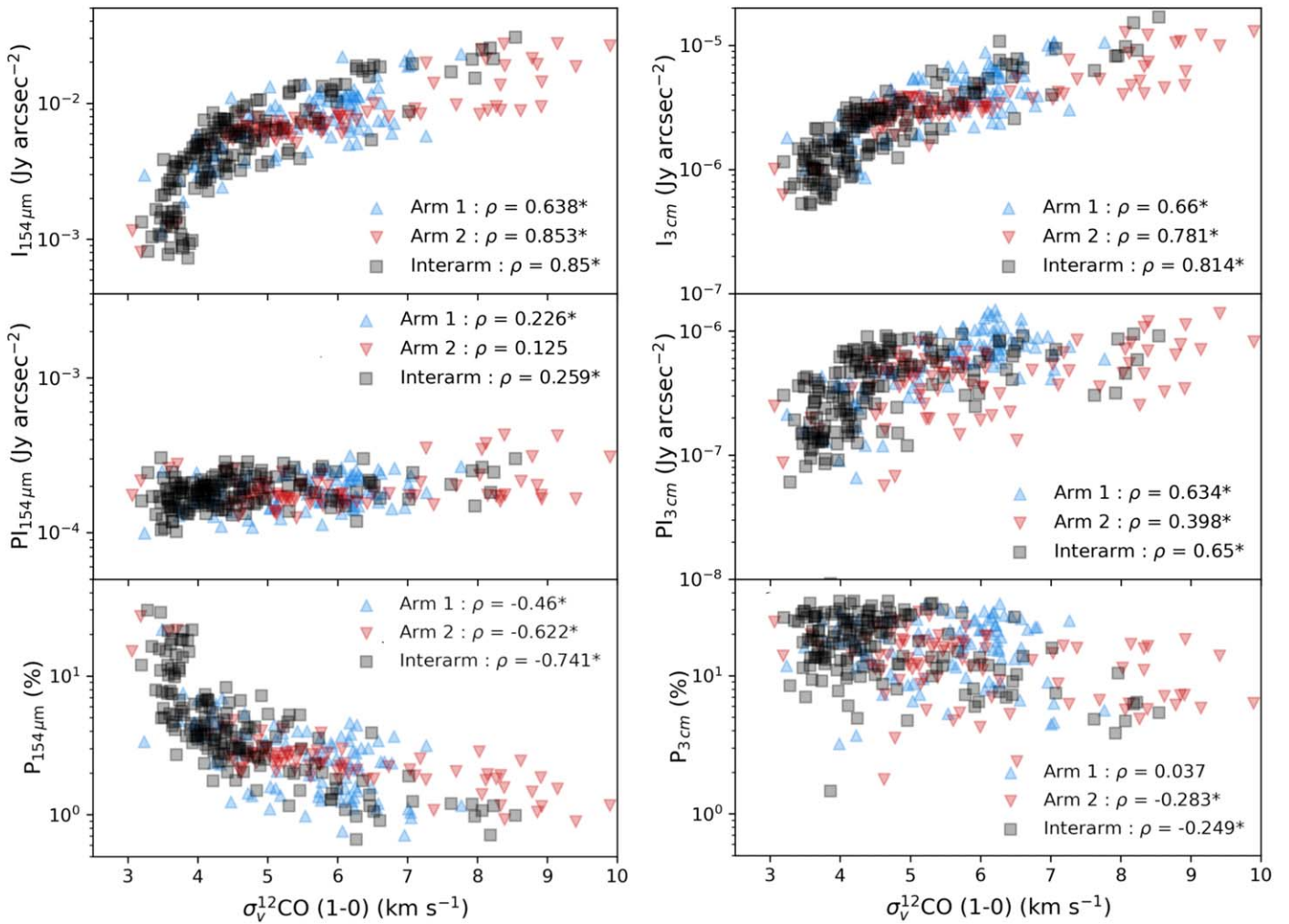**Figure 15.** Comparison between 154 μm (left column) and 3 cm (right column) of the total intensity (top row), polarized intensity (middle row), and polarization fraction (bottom row) as a function of ^{12}CO(1–0) velocity dispersion ($\sigma_{v,^{12}CO(1-0)}$). Arm 1 (blue upward-pointing triangles), arm 2 (red downward-pointing triangles), and interarm (black squares) are as defined in Figure 5. See the legend in each panel for the correlation analysis. An asterisk is shown following the ρ correlation coefficient if the correlation is statistically different from zero ($p < 0.05$).

At radio wavelengths, the total intensity increases with increasing the velocity dispersion of the molecular gas, the polarization fraction is fairly constant across the full range of the velocity dispersion of the molecular gas with $\rho \gtrsim -0.3$, and even this low trend is not statistically significant in arm 1. We find an upward trend in the polarized intensity ($p < 0.05$ in all components). As in the FIR, the radio polarization fraction is higher in the interarm with a probability of $p = 4.7 \times 10^{-3}$ in FIR and $p = 1.2 \times 10^{-4}$ in 3 cm. This result is consistent with the fact that the ^{12}CO(1–0) velocity dispersion is lower in the interarm than in the arms. Fletcher et al. (2011) found an average polarization fraction of up to 40% in the interarm regions against a clearly reduced polarization fraction of up to 25% in the spiral arms.

In Figure 16, we present diagrams for the H I velocity dispersion ($\sigma_{v,H I}$). In general, the results show weaker correlations with H I than with ^{12}CO(1–0) velocity dispersion in FIR and radio. The relation between the total intensity of FIR and 3 cm with $\sigma_{v,H I}$ presents a much lower correlation coefficient, which is only relatively mildly correlated in arm 2 ($\rho \sim 0.5$) but not well correlated in the rest of the components. The results are similar for the polarization fraction and polarized intensity. The FIR polarization intensity does not

show any correlation with $\sigma_{v,H I}$ and is very low in the case of 3 cm. For the polarization fraction, we do not find any significant relation in FIR or 3 cm with the velocity dispersion of H I.

5.2. Star Formation

In this section, we study the relation between star formation in the M51 disk and the magnetic fields. As described in Section 1, one of the hypotheses that could explain the potential differences between FIR and radio polarization maps is the effect of gas turbulence in star-forming regions. As supernova explosions and winds inject the ISM with some level of turbulence, these mechanisms will generate a relationship between turbulence-driven B-fields and SFR. In addition, due to the effects of gravitational collapse, winds, and star formation, the magnetic field in the molecular gas clouds can present systematically different directions when compared to that of the diffuse ISM (i.e., Pillai et al. 2020).

Therefore, SFR-induced turbulence is expected to be a dominant effect. To test this hypothesis, we study the relation between polarization fraction and polarized intensity with the SFR. We obtained the SFR map from Leroy et al. (2019), which
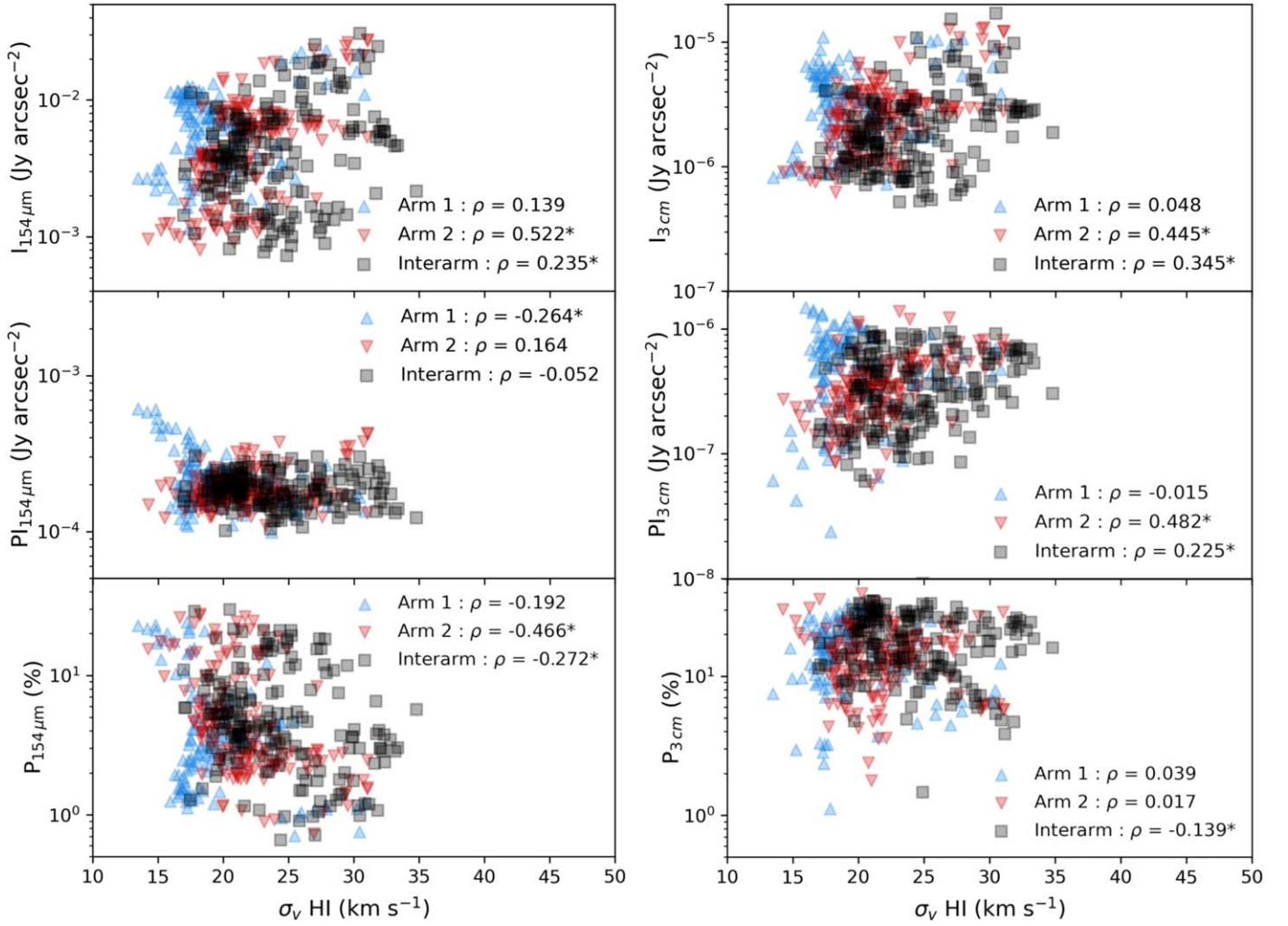
Figure 16. Comparison between 154 μm (left column) and 3 cm (right column) of the total intensity (top row), polarized intensity (middle row), and polarization fraction (bottom row) as a function of H I velocity dispersion ($\sigma_{v,\text{H I}}$). Each data point in arm 1 (blue upward-pointing triangles), arm 2 (red downward-pointing triangles), and interarm (black squares) is a polarization measurement, as in Figure 5. See the legend in each panel for the correlation analysis. An asterisk is shown following each ρ correlation coefficient if the correlation is statistically different from zero ($p < 0.05$).

combined UV, NIR, and mid-IR photometry based on GALEX (Martin et al. 2005), the Wide-field Infrared Survey Explorer (WISE; Wright et al. 2010), and stellar population synthesis models to calibrate integrated SFR estimators. The SFR scales with the ISM density, and this generally decreases with the galactocentric radius. Therefore, to compare different galactocentric radii in an equivalent way, we also normalize the SFR by the surface gas mass density to obtain the SFR efficiency per year. The gas mass density map was calculated by multiplying the column density maps used in Section 5 by the mean molecular weight μ and the hydrogen atomic mass (m_H; see Section 2).

In Figure 17, we show the SFR efficiency analysis for M51. The top panels show the SFR and SFR efficiency maps for the area of M51 (reprojected to the HAWC+ resolution) where we have available FIR and radio observations. As a reference, we display two dashed ellipses at galactocentric radii of 166″ and 183″ (6.9 and 7.6 kpc) as an approximate limiting radius where the magnetic pitch angle profiles of radio and FIR observations are compatible (Section 4.4). On the one hand, the SFR map shows a smooth distribution very similar to the total intensity in FIR, with two well-defined spiral arms and a bright inner region. On the other hand, the SFR efficiency map shows a

clumpy structure, with knots of high efficiency in the outskirts of the spiral arms ($R \sim 150''$, 6.2 kpc) and lower values in the interarms. The bottom panel presents the average SFR efficiency radial profile for the spiral arms of M51. Interestingly, both spiral arms do not show similar trends in SFR efficiency. Arm 2 shows a lower value closer to the galactic center than arm 1. Both arms present noncoincident peaks from the core to the outskirts. We find a decreasing trend in the SFR efficiency of both arms beyond $6.47^{+0.41}_{-0.55}$ kpc ($R_\text{break} = 155.7^{+9.8}_{-13.2}$ arcsec). This change in slope is significant at a $p < 10^{-5}$ level. This might suggest that star formation processes might be playing a role in the same mechanism that produces the systematic differences between the FIR and radio magnetic pitch angle profiles found in Section 4.

In Figure 18, we explore the overall effect of the SFR over the polarization fraction for the HAWC+, 3 cm, and 6 cm data sets. Interestingly, we found that there is a significant anticorrelation between the polarization fraction and the SFR in M51. This correlation is steeper and more correlated in FIR ($\rho = -0.906$) than in radio ($\rho = -0.335$ for 3 cm and -0.540 for 6 cm). For the three wavelengths, the correlation coefficients are significant at a level of $p < 10^{-5}$. Linear modeling of
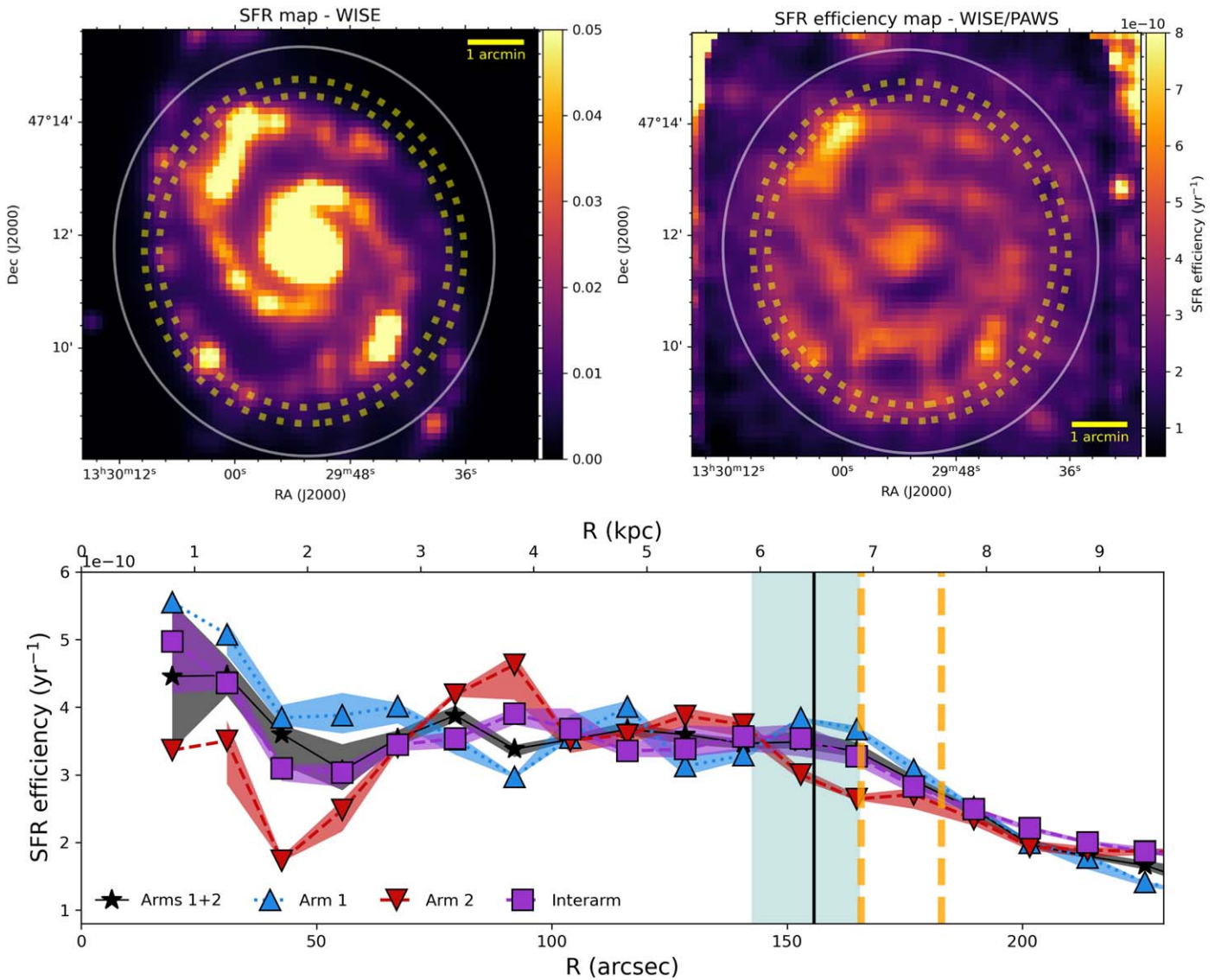
Figure 17. The SFR efficiency analysis of M51. Top left panel: SFR map convolved to HAWC+ resolution from WISE (Leroy et al. 2019). Top right panel: SFR efficiency map estimated from the previous SFR map and the gas mass. Yellow dashed ellipses represent the radii where the magnetic pitch angles from FIR and radio polarization observations decouple in the magnetic pitch angle profiles ($R = 166''$–$183''$; see Figure 8). The white solid ellipse represents the maximum detection radius for HAWC+ observations. Bottom panel: SFR efficiency radial profile based on the two previous maps. Vertical yellow dashed lines represent the $R = 166''$–$183''$ radii. The vertical black solid line and teal rectangle represent the SFR efficiency break median value and its 1σ uncertainty interval, $R = 155.7^{+9.8}_{-13.2}\,''$ ($6.47^{+0.41}_{-0.55}$ kpc). See the legend in the figure.

the log-scaled SFR and polarization fraction diagrams ($\log_{10}(P) = a\log_{10}\mathrm{SFR} + b$) for the different wavelengths shows that the 3 and 6 cm show a variation of P with the SFR shallower than that detected in the FIR data (see Table 4).

We test the SFR correlation against the total and polarized intensity for the radio and FIR in Figure 19. We find that the FIR polarized intensity does not correlate with the SFR ($p = 0.218$), but we find a positive correlation in 3 and 6 cm ($\rho \sim 0.57$ -0.43, $p < 10^{-4}$). We find a positive correlation between the FIR and radio total intensity with the SFR (Table 4). This result is expected due to the FIR–radio correlation (de Jong et al. 1985) and the fact that the SFR is a function of total IR intensity, among other factors (Leroy et al. 2019). For radio, the total intensity increases faster than the polarized intensity with an increase of the SFR across the galaxy.

In conclusion, we have found that there is a significant anticorrelation of the FIR polarization fraction with the SFR in M51, which does not translate into a correlation of the polarized intensity. In contrast, the radio polarized intensity does increase systematically at higher levels of SFR. The linear regression fit for the observed relation between the polarization fraction and SFR is compatible for the 3 and 6 cm observations but not the 154 μm FIR data set of M51. The observations of HAWC+ reveal that the polarization fraction in FIR is highly anticorrelated with the SFR, showing even lower values for the polarization fraction at similar levels of SFR when compared to that predicted by radio observations. For the polarized intensity, we also find a different behavior in the FIR and radio; 3 and 6 cm present a positive correlation between polarized intensity and SFR, while no correlation is observed in 154 μm. We discuss the relevance of these results in Section 6.3.

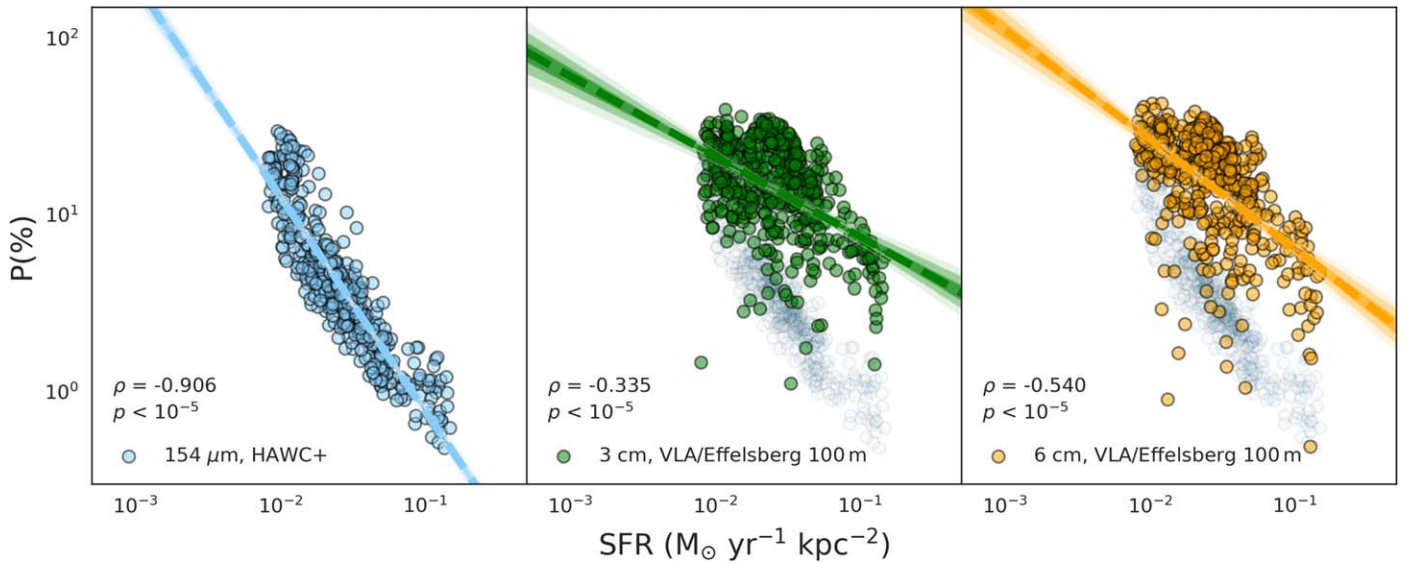**Figure 18.** Polarization fraction as a function of the SFR and wavelength (154 μm, 3 cm, and 6 cm; left to right) for the M51 full disk. Each data point corresponds to an individual pixel position in the HAWC+ and convolved 3 and 6 cm data sets. The dashed line and contours represent the best linear fit to the diagram for each data set. In the background of the middle and right panels, we represent the 154 μm data points for visual reference. See the panels for the statistical correlation tests.

Table 4
Linear Fits to the Relations between Total Intensity (rows 1—3), Polarized Intensity (4–6), and Polarized Fraction (7–9), for μm 154, 3 cm, and 6 cm as a Function of the SFR

ID	Equation	Slope	Intercept
1	$\log_{10} I_{154\,\mu m} - \log_{10} \mathrm{SFR}$	$1.237^{+0.016}_{-0.016}$	$-0.358^{+0.023}_{-0.023}$
2	$\log_{10} I_{3\,cm} - \log_{10} \mathrm{SFR}$	$1.061^{+0.019}_{-0.020}$	$-3.917^{+0.029}_{-0.030}$
3	$\log_{10} I_{6\,cm} - \log_{10} \mathrm{SFR}$	$0.981^{+0.023}_{-0.022}$	$-3.781^{+0.035}_{-0.033}$
4	$\log_{10} PI_{154\,\mu m} - \log_{10} \mathrm{SFR}$	$0.024^{+0.021}_{-0.022}$	$-3.68^{+0.033}_{-0.034}$
5	$\log_{10} PI_{3\,cm} - \log_{10} \mathrm{SFR}$	$0.603^{+0.039}_{-0.038}$	$-5.49^{+0.063}_{-0.061}$
6	$\log_{10} PI_{6\,cm} - \log_{10} \mathrm{SFR}$	$0.360^{+0.038}_{-0.037}$	$-5.59^{+0.061}_{-0.063}$
7	$\log_{10} P_{154\,\mu m} - \log_{10} \mathrm{SFR}$	$-1.212^{+0.028}_{-0.029}$	$-1.32^{+0.044}_{-0.044}$
8	$\log_{10} P_{3\,cm} - \log_{10} \mathrm{SFR}$	$-0.455^{+0.036}_{-0.033}$	$0.420^{+0.058}_{-0.054}$
9	$\log_{10} P_{6\,cm} - \log_{10} \mathrm{SFR}$	$-0.620^{+0.037}_{-0.036}$	$0.185^{+0.061}_{-0.061}$
10[a]	$\log_{10} P_{154\,\mu m} - \log_{10} I_{154\,\mu m}$	$-0.979^{+0.016}_{-0.018}$	$-1.670^{+0.036}_{-0.041}$

[a] Results for the $P_{154\mu m}$ vs. $I_{154\mu m}$ model.

6. Discussion

6.1. FIR versus Radio Magnetic Fields

In this work, we find that the magnetic pitch angles at radio (3 and 6 cm) and FIR (154 μm) are well aligned in the inner $R < 160''$ (<6.7 kpc) radius of M51, i.e., $R < 160''$: $\Psi_{FIR} \sim \Psi_{3\,cm} \sim \Psi_{3\,cm}$. This result does not change when considering each of the spiral arms independently or combined, using only the interarm region, or analyzing the complete disk of M51 at once. Only for the interarm region are the FIR and radio magnetic pitch angles similar up to the largest radius ($220''$, 9.15 kpc) of our observations, i.e., $R \leqslant 220''$: $\overline{\Psi}^{IA}_{FIR} \sim \overline{\Psi}^{IA}_{3\,cm} \sim \overline{\Psi}^{IA}_{6\,cm}$. We find a significant difference between the magnetic pitch angles of the arms at radio and FIR in the outer region ($R > 160''$; > 6.7 kpc) of M51, i.e., $R > 160''$: $\overline{\Psi}^{Arms}_{FIR} < \overline{\Psi}^{Arms}_{3\,cm} \sim \overline{\Psi}^{Arms}_{6\,cm}$. In the outskirts of M51, the FIR magnetic spiral arms are wrapped tighter than the radio ones. The radio magnetic pitch angle seems to be more open at increasing radius from the core. Our study provides the

first observational evidence of a morphological difference between the kiloparsec-scale magnetic field structure of radio and FIR in external galaxies.

We find that the morphological and magnetic pitch angles vary as a function of the ISM component such as $\overline{\Psi}^{Morph}_{H\,I} < \overline{\Psi}^{Morph}_{CO} < \overline{\Psi}^{Morph}_{FIR} \sim \overline{\Psi}^{Morph}_{3\,cm} \sim \overline{\Psi}^{Morph}_{6\,cm}$ (see Section 4.4). The spiral arms traced by the neutral gas (H I) are wrapped tighter than those traced by the molecular gas observed in ^{12}CO(1–0). Interestingly, the morphological pitch angles at radio and FIR are the same across the full extent ($220''$, 9.15 kpc) of the galaxy, i.e., $\overline{\Psi}^{Morph}_{FIR} \sim \overline{\Psi}^{Morph}_{3\,cm} \sim \overline{\Psi}^{Morph}_{6\,cm}$. However, the magnetic and morphological angles show different behavior across the galaxy disk. At low radii ($R < 120''$, $R < 5.0$ kpc), $\Psi^{Morph}_{FIR,3\,cm,6\,cm} > \Psi_{FIR,3\,cm,6\,cm}$, while at larger radii, $\Psi^{Morph}_{FIR,3\,cm,6\,cm} < \Psi_{FIR,3\,cm,6\,cm}$. The exception is at FIR at radii $R > 190''$ (>7.9 kpc), where $\Psi^{Morph}_{FIR} > \Psi_{FIR}$. Although radio and FIR may be tracing the same morphological regions of the galaxy disk, we found that the magnetic pitch angle of the FIR differs at the outskirts of the galaxy. The FIR may be affected by a different physical mechanism in the outer regions of M51 (see Section 6.2).

The statistical difference found between the morphological and magnetic pitch angles in the disk of M51 at the three wavelengths analyzed may be a direct hint of the independence of the α–Ω dynamo from the spiral density waves (Beck 2015b). Differences between the magnetic and morphological pitch angles have been repeatedly found by previous authors; the average magnetic pitch angle of M83 is about 20° larger than that of the morphological spiral arms (Frick et al. 2016). In M101, the ordered magnetic pitch angle is found to be ~8° larger than those from the morphological pitch angle of the H I structures (Berkhuijsen et al. 2016). Van Eck et al. (2015) found that, on average, the magnetic pitch angle is ~5°–10° more open than the morphological pitch angles using a sample of 20 nearby galaxies, a conclusion also found by Mulcahy et al. (2017) in M74.
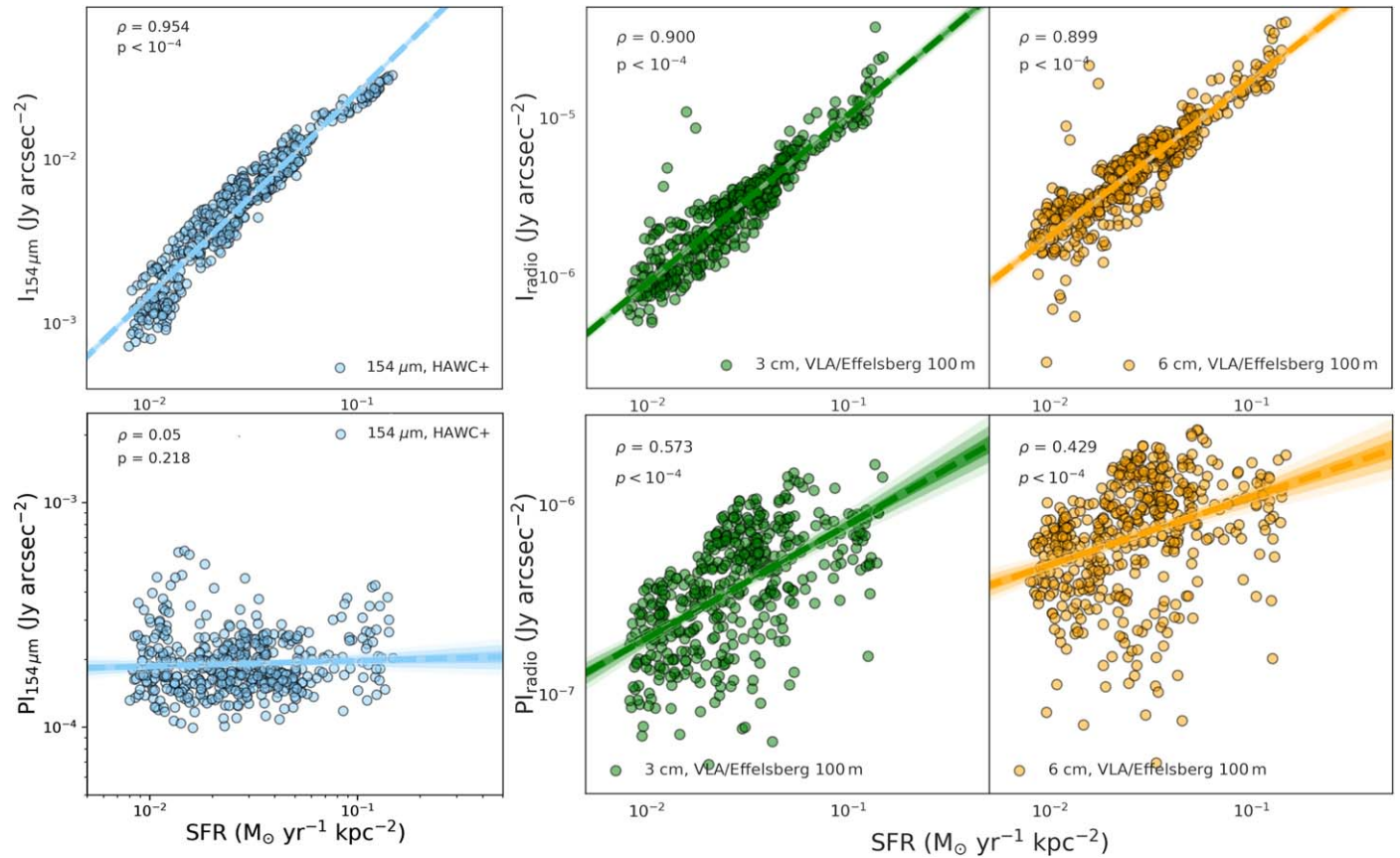
Figure 19. Total (top) and polarized intensity (bottom) as a function of the SFR and wavelength (154 μm, 3 cm, and 6 cm; left to right) for the M51 full disk. Linear fits are presented in Table 4. See the panels for the statistical correlation tests.

In theory, spiral magnetic fields can be compressed by density waves, modifying the magnetic pitch angle. This mechanism would create a difference in the arm–interarm region across the galaxy disk. The regular magnetic field in the spiral arm should be more similar to that of the morphological pitch angle than the interarm magnetic field. The magnetic pitch angle may be first compressed and ordered in the interface between the arm and interarm regions. There may be a temporary and spatial disconnect between the morphological and magnetic spiral arms due to the relative action of the large- and small-scale dynamos. Detailed modeling of the M51 galactic system based on these observations would be required to test the interaction of the spiral density waves with the α–Ω dynamo.

6.2. The Magnetic Fields in the Multiphase ISM

In Section 5, we find that the radio and FIR total intensity emission are both tightly correlated with the column density $N_{\mathrm{H\,I+2H_2}}$ and the ^{12}CO(1–0) velocity dispersion. This result and the implicit radio–FIR correlation were explained by Niklas & Beck (1997). In addition, we find that the FIR polarization decreases with increasing the velocity dispersion of the molecular gas and increasing column density. The interarm shows lower velocity dispersion and a higher degree of polarization than the arms. As the velocity dispersion is used as a proxy for the turbulent kinetic energy in the disk, a possible interpretation is that the small-scale turbulent magnetic field may be relatively more significant at a higher velocity

dispersion of the molecular gas and column densities than the large-scale ordered field.

In addition, our results show that the FIR and radio total intensity, polarized intensity, and polarization fraction do not correlate with turbulence in H I. Using magnetohydrodynamic simulations, Dobbs & Price (2008) suggested that the small-scale turbulent component is produced by the velocity dispersion of the dust and cold gas. This turbulent component would be generated by the passage through a spiral shock. The authors found that without the cold gas component, the B-field remains well ordered apart from being compressed in the spiral shocks. Our results suggest that the small-scale turbulent field is then coupled to the molecular gas motions but not to the neutral gas of M51. The molecular gas motions are more concentrated in the densest regions of the spiral arm and spatially coincident with the star-forming regions along the arms.

These results suggest that the regions with higher column densities and levels of turbulence of the molecular gas ^{12}CO(1–0) reduce the measured FIR polarization fraction inside each beam. The polarized intensity is not affected by these quantities. The polarization fraction at radio wavelengths seems to be insensitive to the column density and the level of turbulence of the molecular gas; instead, the polarized radio emission is affected by these quantities. We find that both FIR and radio are insensitive to the turbulence in the neutral gas (H I) across the galaxy disk. Interestingly, Beck et al. (2019) found no evidence of a spiral modulation of the

rms turbulent speed when comparing the velocity dispersion of H I with the radio polarization of several spiral galaxies (M51 included).

6.3. Star Formation and Magnetic Fields

In Section 5.2, we find a systematic anticorrelation between the polarization fraction and the SFR. Similar results were obtained earlier by Frick et al. (2001; using H_α emission and 6.2 cm radio polarization) and Tabatabaei et al. (2013) in NGC 6946. The results of our work indicate that both the FIR and radio polarization fraction are anticorrelated with the SFR. Interestingly, the polarized intensity at $154 \, \mu$m shows a negligible correlation with the SFR, $N_{\rm H\,I+2H_2}$, and ^{12}CO(1–0) velocity dispersion, whereas the polarized intensity increases at 3 and 6 cm. In the diffuse ISM, the polarization fraction will decrease due to (1) an increase of the relative contribution of unpolarized thermal emission from SFR, (2) Faraday depolarization, and (3) variations of the B-field orientation within the beam and along the LOS. Processes related to star formation (small-scale dynamo) would induce the formation of an anisotropic B-field component from the isotropic turbulent field, hence increasing the polarized intensity in 3 and 6 cm. The polarized intensity may increase if the relative contribution of anisotropic turbulent fields increases within the beam. However, the polarized intensity distributions in FIR show no correlation with SFR, $N_{\rm H\,I+2H_2}$, or turbulence. Two different scenarios may explain this result.

1. Different magnetic field directions in the same LOS or within the same beam decrease the polarization intensity in FIR (Fissel et al. 2016).
2. Dust grain alignment efficiency depends on the total intensity, especially toward regions of high column density (Hoang et al. 2021).

In the first scenario, the turbulence and morphological complexity of the B-field in and around the molecular clouds may cause beam depolarization at FIR wavelengths. Considering this hypothesis, the relative physical size of the HAWC+ beam at $154 \, \mu$m is $13''6$, approximately 565 pc at a distance of 8.58 Mpc. If we compare this with the size distribution of the giant molecular clouds of M51, which range from 9 to 190 pc in radius, with an average of $\sim$50 pc (Hughes et al. 2013), we find that the vast majority of these clouds and their structure are unresolved with our spatial resolution. Thus, the complex B-field in the POS within our beam and/or tangled B-field along the LOS toward the cores of these structures causes a drop of polarization in our observations (i.e., depolarization).

The second proposed mechanism is based on a loss of dust grain alignment efficiency toward regions of high column density and gas turbulence. According to the RATs (Dolginov & Mitrofanov 1976; Lazarian & Hoang 2007), dust grain alignment efficiency decreases for grains smaller than a certain size ($a_{\rm crit}$) with column density due to the collision dumping effect (Hoang et al. 2021). Specifically, higher gas density causes a stronger loss of alignment by gas collision (which affects smaller grains more efficiently). This effect changes the population of aligned grain sizes to larger dust grains, i.e., the grain-size distribution of aligned grain is narrower, which makes polarization fraction decrease with increasing intensity and $N_{\rm H\,I+2H_2}$. In addition, polarization fraction decreases with

increasing gas turbulence (velocity dispersion of gas) because the gas turbulence randomizes and/or changes the PA of polarization along the LOS. This effect results in a decrease of polarization fraction as $\sigma_{v,^{12}{\rm CO}(1-0)}$ increases, consistent with the first proposed scenario considering RATs.

To quantify this effect, the polarization fraction has been found to depend on a certain power of the total intensity (P $\propto$ I$^\xi$; Hoang et al. 2021). The power depends on the dust grain alignment efficiency, where $\xi = 0$ corresponds to full alignment (perfectly polarized dust grain population), $\xi = -1$ to pure random alignment, and $\xi = -0.5$ to alignment dominated by gas turbulence. As PI $=$ P $\cdot$ I, polarized intensity becomes constant as ξ decreases. In the case of M51, we measure $\xi = -0.979^{+0.016}_{-0.018}$ (see Table 4), which implies a pure random alignment regime. In this regime, polarized intensity is constant with total intensity, $N_{\rm H\,I+2H_2}$, and $\sigma_{v,^{12}{\rm CO}(1-0)}$.

These hypotheses for the variation of the polarization fraction of intensity, as well as the lower anticorrelation found in radio observations when compared to FIR, require further investigation, which is beyond the scope of this manuscript.

We cannot directly connect the variation of the polarization fraction with the inner structure of the magnetic field in radio. In order to do that, we would need to take into account the added factor of Faraday depolarization (Sokoloff et al. 1998) and the increase in unpolarized thermal emission, which can be significant at 3 and 6 cm. Regions with higher SFR present higher molecular gas densities, cold gas velocity dispersion, and higher neutral gas column densities. This can be associated with a decrease in the polarization fraction in FIR but also an increase of the total FIR intensity.

The SFR efficiency profile does show a significant decrease at $R = 155.7^{+9.8}_{-13.2}''$ ($6.47^{+0.41}_{-0.55}$ kpc) of the galactic disk. The different SFR efficiency profiles between both arms suggest an asymmetric structure, possibly triggered by the interaction of the galactic disk with the companion galaxy, M51b. In addition, we do not observe the misalignment of the FIR magnetic field outside the spiral arms. This distortion is found in the outermost radius of M51, close to the radii where arm 2 is closer to M51b. While there is an agreement of the general structure between the magnetic field of the spiral arms in the molecular gas and the diffuse ISM for the inner region, the magnetic pitch angle break is only found in the FIR and not the radio polarization observations. These results may suggest that the molecular disk might be more affected by the interaction with M51b than the diffuse gas. This result is expected, since the molecular gas is a kinematically colder component of the galactic disk than the diffuse, more dispersion-supported gas. Iono et al. (2005) found significant differences ($\Delta v > 50$ km s^{-1}) between the diffuse gas and molecular disk kinematics in the rotation curves of a sample of galaxy interacting pairs observed in H I and CO. This suggests that the distortion of the magnetic pitch angle profile found in the outskirts could be produced by the interaction of M51b with the cold dense molecular disk, visible on both sides of the galaxy due to the effect of gravitational tidal forces (Duc & Renaud 2013). Galaxy interactions could affect the diffuse gas differently from the molecular gas, which is kinematically colder, with a highly rotation-supported distribution (Drzazga et al. 2011). In that case, the location of the molecular clouds preferentially in the spiral arms of M51 could explain the finding of a misalignment between the two components of the magnetic field. Indeed, a

large angular dispersion in the measured magnetic field due to the interaction of galaxies has recently been found using 89 μm polarization data of Centaurus A by Lopez-Rodriguez (2021). This author found that the small-scale turbulent fields have a larger contribution than large-scale ordered fields in the molecular gas of the remnant warped disk. The fact that we find the distortion on both spiral arms will require a detailed magnetohydrodynamic study of the effects of tidal forces on galactic disks and the previous history of the M51 interaction. The most drastic feature is the down-bending break of the magnetic pitch angle profile in FIR.

Van Eck et al. (2015) and Chyży et al. (2017) found a tight relationship between the specific SFR and the total magnetic field strength, which implies that the process of amplifying magnetic fields in galaxies is mainly driven by small-scale dynamo mechanisms from the local SFR (Gressel et al. 2008a; Schleicher & Beck 2013). The results from Chyży et al. (2017) show that the total magnetic field is correlated with the density of the cold molecular gas (H$_2$) but not with the warm diffuse H I ISM, a result that is compatible with our findings in Section 5. This shows that the amplification of the B-fields may be taking place in the star-forming regions of M51. This amplification may be driven by small-scale turbulent dynamos, where small-scale refers to scales smaller than our beam size and spatially correlated with the star-forming regions along the spiral arms.

7. Conclusions

One of the most important and unexplored questions in galaxy evolution is, Can magnetic fields shape galaxies? (Battaner & Florido 2007; Ruiz-Granados et al. 2010, 2012; Tsiklauri 2011; Jałocha et al. 2012a, 2012b; Elstner et al. 2014). Previous analyses of this topic based their conclusions on the structure of the radio polarization magnetic field, corresponding to the diffuse ISM. In this paper, we present quantitative evidence that the kiloparsec-scale structure of the magnetic field in the molecular gas and the diffuse ISM of the grand design face-on spiral galaxy M51 shows significant differences in the structure.

1. Within the inner 150″ (6.24 kpc) of M51, we found a general agreement of the magnetic field orientation (measured as the magnetic pitch angle) between the 154 μm and the 3 and 6 cm bands. At $R > 150″$ (>6.24 kpc), the magnetic pitch angle profile at 154 μm shows a significant break toward lower pitch angles, which is not detectable in 3 or 6 cm.
2. When the two individual spiral arms are compared, they consistently show significantly different magnetic pitch angle profiles at all three wavelengths studied. The exception is found at the outer region ($R > 150″$, >6.24 kpc) in 154 μm.
3. Longer wavelengths have higher magnetic pitch angles in the arms, i.e., $\Psi_{\text{FIR}}^{\text{Arms}} < \Psi_{3\,\text{cm}}^{\text{Arms}} \sim \Psi_{6\,\text{cm}}^{\text{Arms}}$.
4. We do not find significant differences in the magnetic pitch angles of the interarm regions, i.e., $\Psi_{\text{FIR}}^{\text{IA}} \sim \Psi_{3\,\text{cm}}^{\text{IA}} \sim \Psi_{6\,\text{cm}}^{\text{IA}}$.
5. The morphological pitch angles at FIR and radio wavelengths are similar across the full disk of M51. However, we found that morphological pitch angles change as a function of the multiphase ISM, such as $\Psi_{\text{H I}}^{\text{Morph}} < \Psi_{\text{CO}}^{\text{Morph}} < \Psi_{\text{FIR}}^{\text{Morph}} \sim \Psi_{3\,\text{cm}}^{\text{Morph}} \sim \Psi_{6\,\text{cm}}^{\text{Morph}}$.
6. At FIR, radio, and radius $<100″$ (<4.16 kpc), the magnetic pitch angles are wrapped tighter than the morphological pitch angles.
7. At FIR, radio, and radius $>100″$ (>4.16 kpc), the magnetic pitch angles of the spiral arms are larger than those from the morphological structure. The exception is FIR, whose magnetic pitch angle becomes tighter than the morphological pitch angle at radius $>200″$ (>8.32 kpc).

We also compared the FIR and radio polarization with the properties of the multiphase ISM using the column density, the velocity dispersion of the neutral (H I) and molecular (^{12}CO(1–0)) gas, and the SFR. Our results are as follows.

1. The FIR and radio total intensity are positively correlated with the hydrogen column density and ^{12}CO(1–0) velocity dispersion.
2. The FIR polarization fraction is negatively correlated with the total hydrogen column density ($N_{\text{H I}+2\text{H}_2}$) and the ^{12}CO(1–0) velocity dispersion. At radio, the polarization fraction is flat with these quantities.
3. The FIR polarized intensity is flat with the column density and ^{12}CO(1–0) velocity dispersion. At radio, the polarization intensity increases with these quantities. Two different mechanisms (beam depolarization and dust grain alignment efficiency) are proposed in Section 6.3 to explain the different trends observed in FIR.
4. We found no correlation between FIR and radio with the H I velocity dispersion.
5. The polarization intensity presents a significant correlation with the SFR in 3 and 6 cm but none in 154 μm observations. We found a tight anticorrelation between the polarization fraction and SFR in 154 μm and 3 and 6 cm.
6. The two spiral arms show different trends as a function of SFR efficiency. Arm 2 shows a lower value closer to the galactic center than arm 1. Both arms present noncoincident peaks from the core to the outskirts.
7. We found a decreasing trend in the SFR efficiency of both arms beyond $7.0_{-0.8}^{+0.7}$ kpc ($R_{\text{break}} = 167_{-20}^{+17}$ ″).

The results detailed above point to an important observation: the multiphase of the ISM affects the B-field structure in the galaxy. This effect can be disentangled with a multiwavelength approach using the FIR and radio polarization observations. Our observations support the presence of a clear interlinked scenario between the SFR and the magnetic field in different phases of the ISM. Lower polarization fractions may be due to the presence of magnetized but complex structures in the regions with denser molecular clouds. The locations of the arm, interarm, and core components used to produce the diagrams of polarization fraction and intensity support this interpretation.

The diffuse ISM presents a much more regular magnetic field than the cold dense molecular gas, and this is revealed in the structure of the magnetic pitch angle profiles. It is interesting that these magnetic fields show differences from the pitch angle structure of the morphological arms, supporting the separation of the α–Ω dynamo from the density waves. The observed differences between the radio parameters and those of the FIR might be produced by kinematic decoupling between the diffuse and dense ISM through tidal forces with the companion galaxy M51b. However, other effects, such as internal kinematic phenomena associated with density wave resonances, cannot be ruled out. These effects are beyond the

scope of this paper and will be studied in a forthcoming publication.

It remains unknown if the magnetic fields can systematically influence the global kinematics of the star-forming regions inside the molecular clouds, enhancing stellar migration. Observational testing of such a hypothesis can only be obtained through a revision of our analysis based on the magnetic field structure of molecular clouds in galaxies. High-resolution FIR polarization observations of galaxies such as those provided by HAWC+/SOFIA are vital to understanding the role of magnetic fields in the evolution of the universe. Ongoing efforts like the SOFIA Legacy Program (PIs: Lopez-Rodriguez & Mao) will provide deeper FIR polarimetric observations of a sample of nearby galaxies, where, combining them with observations of radio and other tracers, we should be able to disentangle the relation between the SFR and the magnetic structure of the molecular clouds within the galactic disks.

Appendix A
Mock Magnetic Field Test

In this section, we detail the tests performed to ensure the quality of the magnetic pitch angle profiles. We use a set of eight mock observations with different configurations in terms of magnetic pitch angle (Ψ), PA, inclination (i), and S/N. These tests were performed following a single-blind setup, where a member of the team produced the mock observations and another member of the team performed the data analysis without knowing the parameters of the models. This approach ensures the unbiased quality of the results. We use the 89 μm HAWC+ observations of NGC 1068 presented by Lopez-Rodriguez et al. (2020) to set up the HAWC+ array configuration and the total intensity. Figures 20 and 21 show the total intensity of NGC 1068 at 89 μm. Stokes QU were replaced by the mock observations with the parameters shown in Table 5. A logarithmic spiral function with a single pitch angle, Ψ, across the image was used. This B-field model was then inclined and tilted to produce the projected B-field orientation in the POS. Noise was added using a Gaussian profile with mean $\mu = 0$ and standard deviation $\sigma = \max(IQU)/$ S/N; that is, the noise level is specified by the desired S/N from the peak pixel. Figure 22 shows the difference between the fixed parameter in the model with the estimated pitch angle following the approach in Section 3.1. An accuracy of $\leqslant 5°$ is achieved for polarization measurements with $P/\sigma_P \geqslant 2$. The large uncertainties at the inner and outer radii are due to the small number of polarization measurements producing enough statistical analysis. At these radii, a maximum angular uncertainty of $\sim 15°$ is expected.
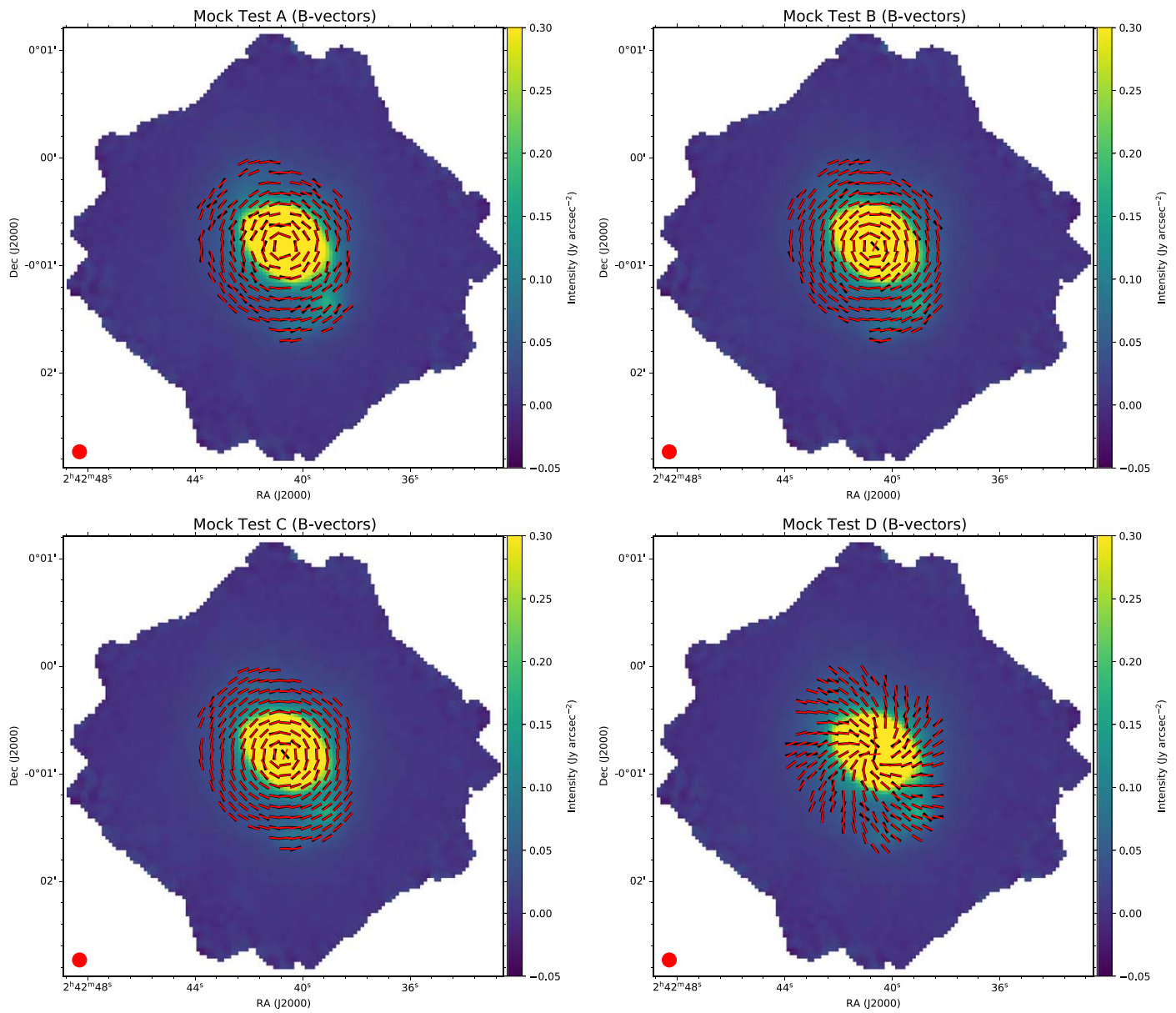
Figure 20. Mock observations of the spiral B-field. Total intensity (color scale) maps show the 89 μm HAWC+ observations of NGC 1068 by Lopez-Rodriguez et al. (2020). Mock B-field orientations (black) and the model (red) are shown for tests ABCD with the parameters shown in Table 5.
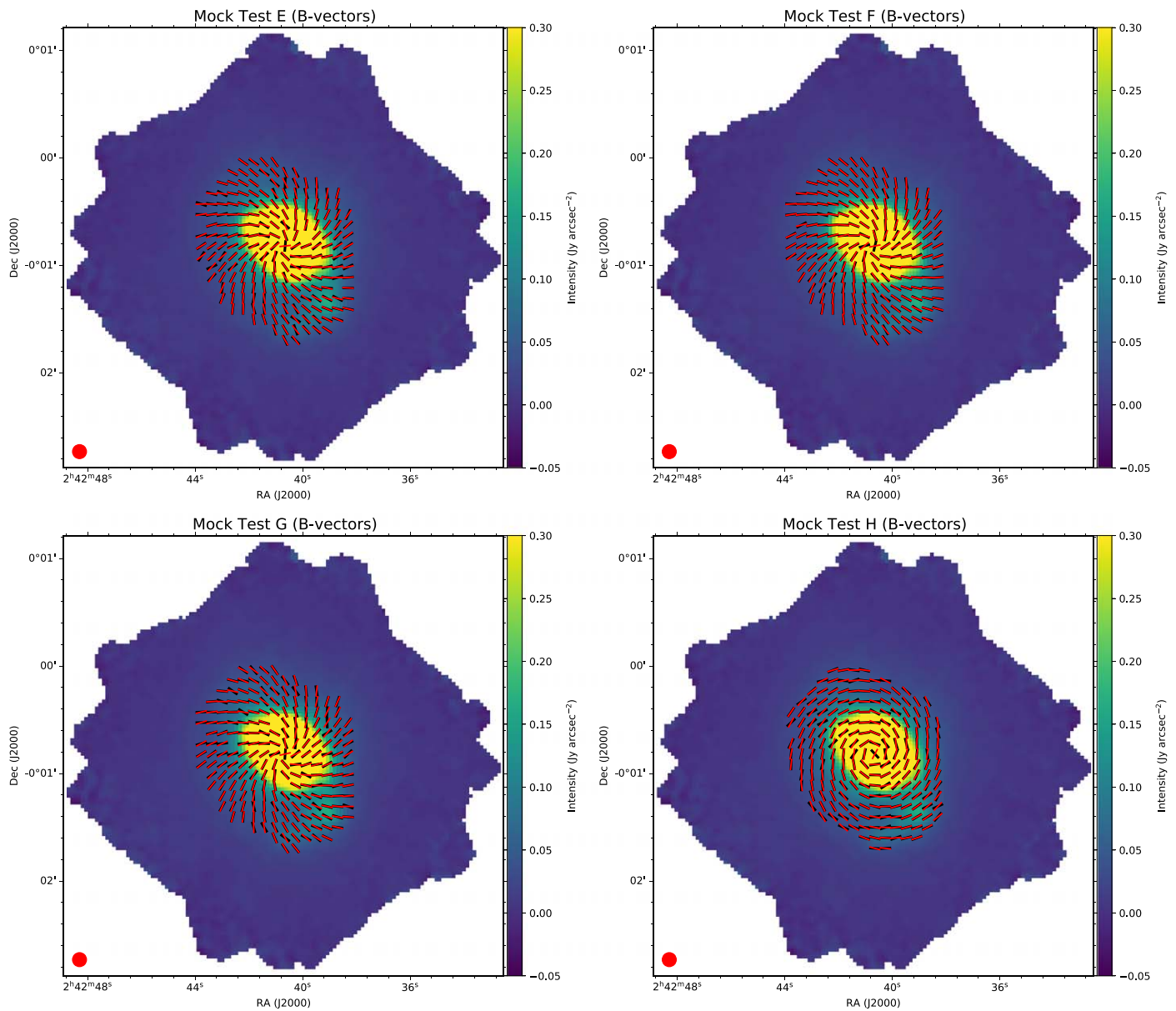
Figure 21. Same as Figure 20 but for tests EFGH.

Table 5
Parameters of Mock Observations for the Pitch Angle Estimations

Test	Inclination (deg)	PA (deg)	Pitch (deg)	S/N	Comments
(1)	(2)	(3)	(4)	(5)	(6)
A	0	0	0	1	Face-on, azimuthal profile, low S/N
B	0	0	0	3	Face-on, azimuthal profile
C	0	0	0	10	Face-on, azimuthal profile, high S/N
D	0	0	60	1	Face-on, large pitch angle, low S/N
E	0	0	60	3	Face-on, large pitch angle
F	0	0	60	10	Face-on, large pitch angle, high S/N
G	30	0	60	1	Inclined, large pitch angle, low S/N
H	30	47	17	1	Inclined, tilted, small pitch angle, low S/N

Note. Columns: (1) ID, (2) inclination of the model, (3) PA, (4) *B*-field pitch angle, (5) S/N, (6) brief description of the individual models.
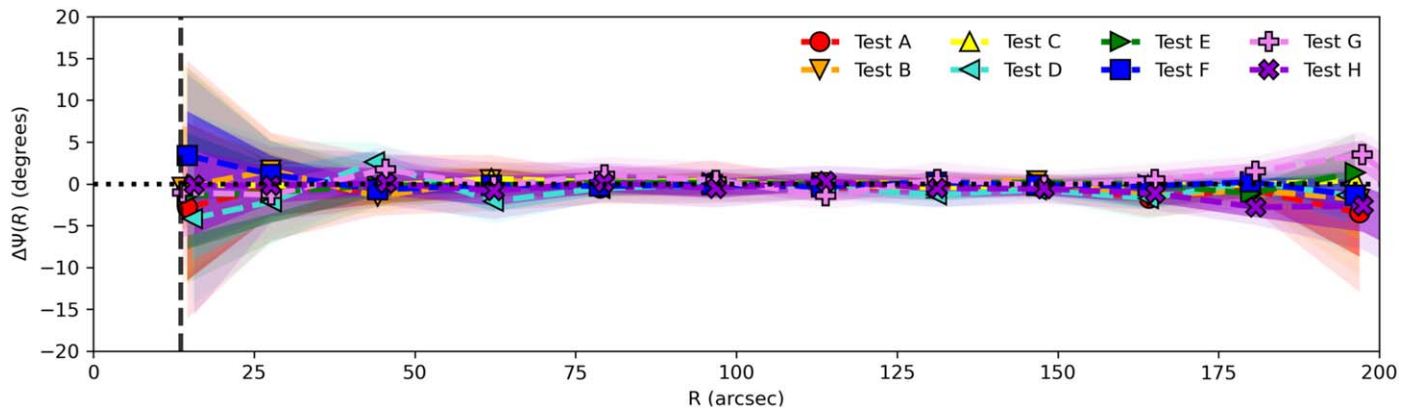
Figure 22. Magnetic pitch angle mock data set analysis. On the vertical axis, we represent the magnetic pitch angle profile $\Psi(R)$ minus the simulated angle Ψ_{mock} as a function of radius for the mock observations shown in Table 5.

Appendix B
Polarization PA Diagrams

In Figure 23, we represent the PAs of the 90°-rotated polarization orientations of the 3 and 6 cm radio data sets as a function of those of SOFIA/HAWC+ in 154 μm for the different morphological components of M51. We refer to

Figure 11 of Jones et al. (2020) for a version of this figure with a subset of the HAWC+ observations presented in this work. The observed variation from a 1:1 relation is expected in these diagrams, suggesting that FIR and radio polarization observations do not trace the same magnetic field structure, agreeing with the main results of the present work (see Section 7).
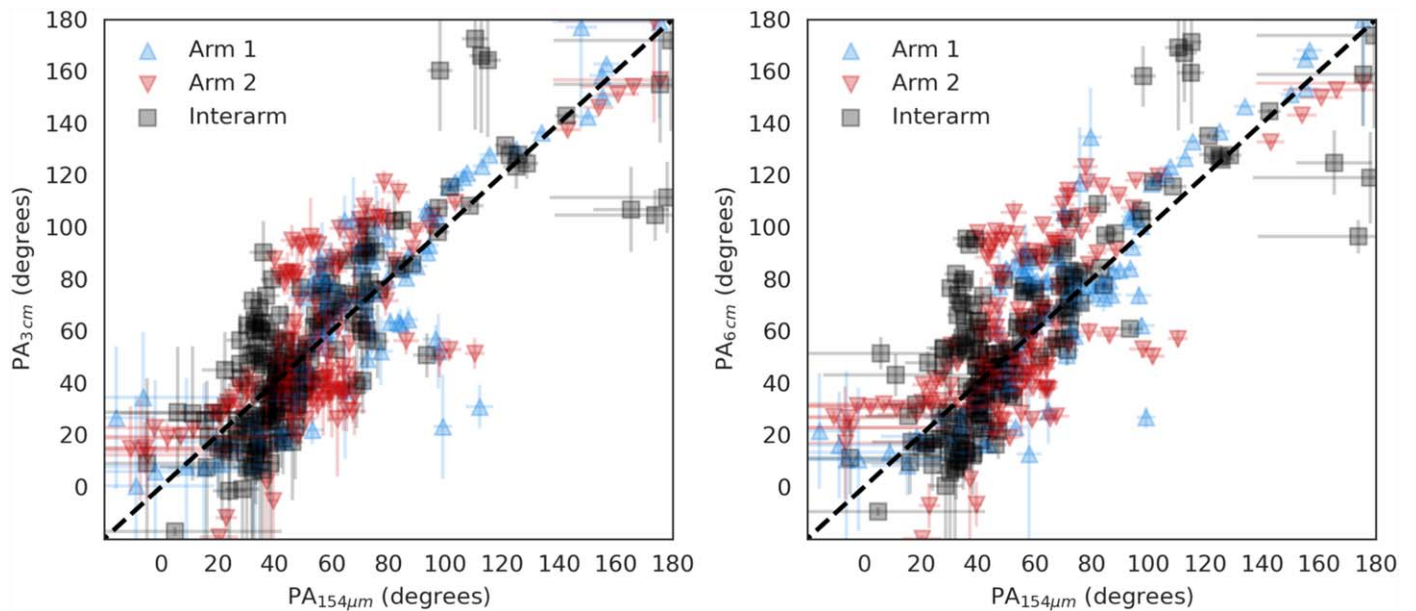

Figure 23. Distribution of the PAs of the 90°-rotated polarization orientations in 3 and 6 cm as a function of those obtained in 154 μm. The dashed diagonal line represents the 1:1 relation. See the legend for the symbols identifying the different morphological components of M51.

Appendix C
Polarization Diagrams at 6 cm

In this appendix, we show the plots for the total intensity, polarized intensity, and polarization fraction at 6 cm as a function of the column density and velocity dispersion of the molecular gas ^{12}CO(1–0) (Figure 24), and the neutral gas H I (Figure 25). Section 5 presents the analysis.
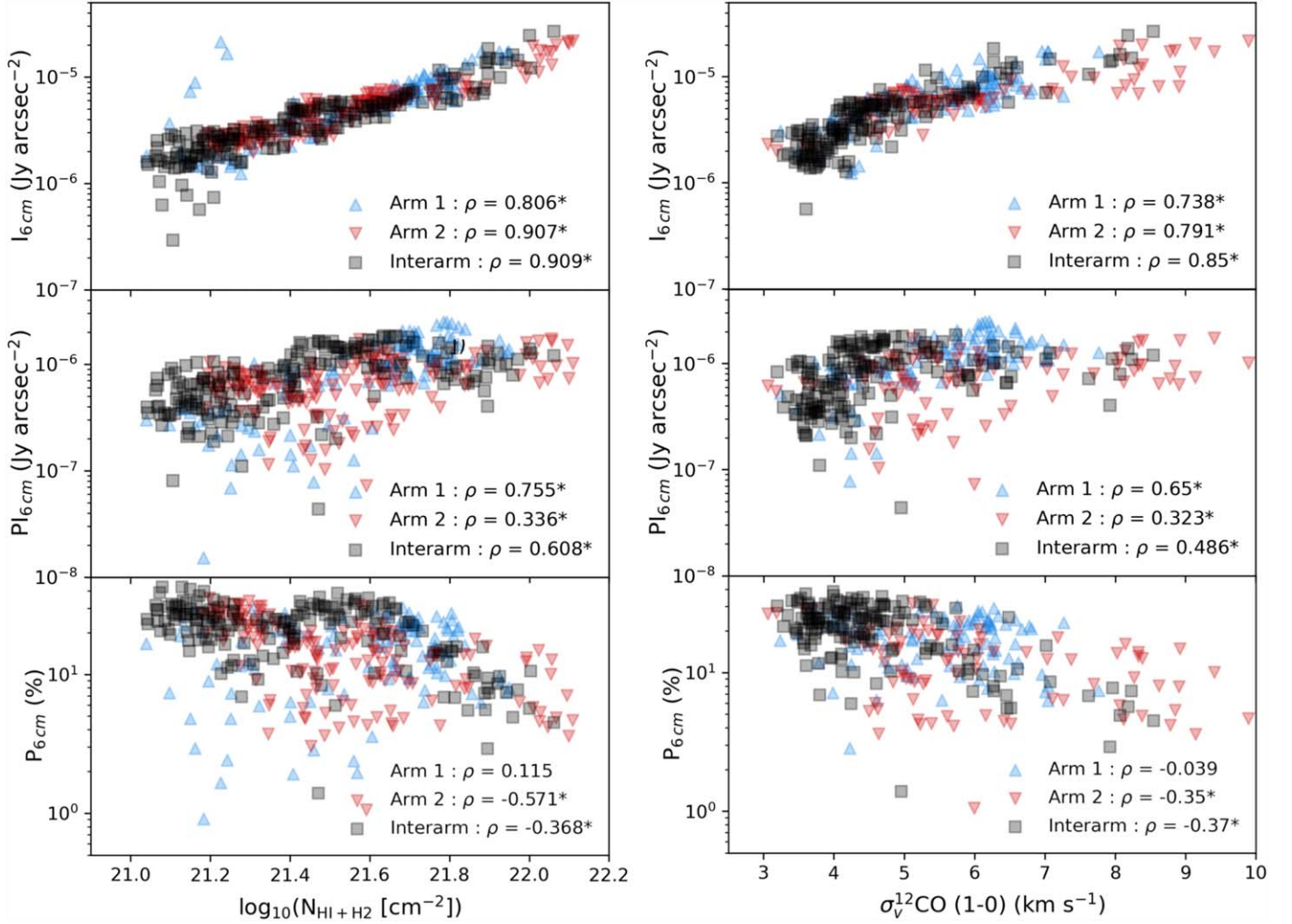

Figure 24. Distribution of 6 cm total intensity (top row), polarized intensity (middle row), and polarization fraction (bottom row) as a function of gas column density ($N_{\rm H I+2H_2}$; left column) and ^{12}CO(1–0) velocity dispersion ($\sigma_{v,^{12}CO(1-0)}$; right column). Symbols represent arm 1 (blue upward-pointing triangles), arm 2 (red downward-pointing triangles), and the interarm region (black squares), where each data point is a polarization measurement as shown in Figure 5. See the legend in each panel for the correlation analysis. An asterisk is shown following the ρ correlation coefficient if the correlation is statistically different from zero ($p < 0.05$).
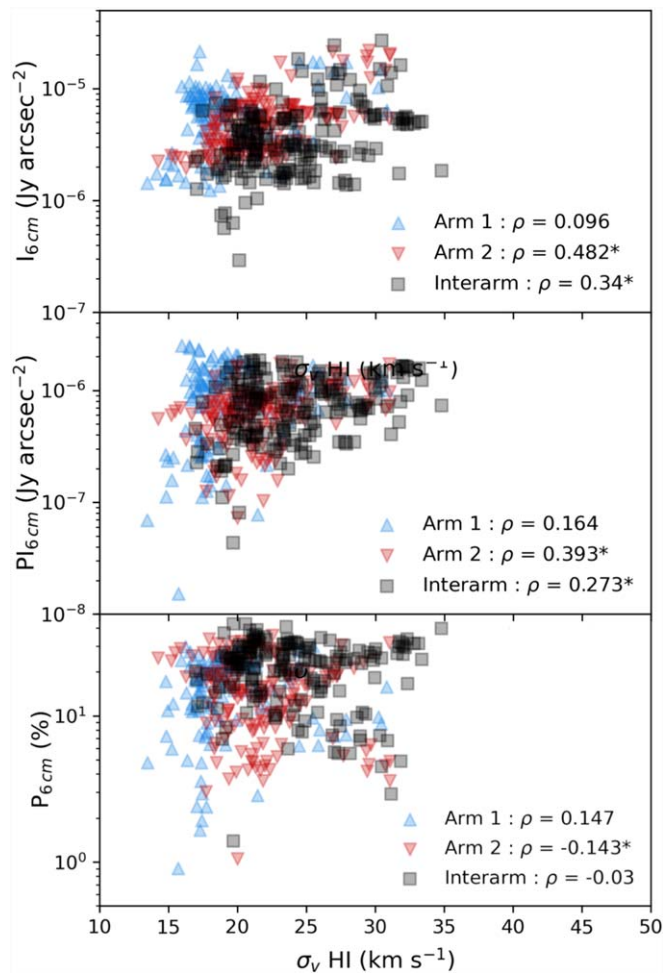
Figure 25. Distribution of 6 cm total intensity (top row), polarized intensity (middle row), and polarization fraction (bottom row) as a function of the H I velocity dispersion ($\sigma_{v,\text{H I}}$). Symbols represent arm 1 (blue upward-pointing triangles), arm 2 (red downward-pointing triangles), and the interarm region (black squares), where each data point is a polarization measurement as shown in Figure 5. See the legend in each panel for the correlation analysis. An asterisk is shown following the ρ correlation coefficient if the correlation is statistically different from zero ($p < 0.05$).

ORCID iDs

Alejandro S. Borlaff ● https://orcid.org/0000-0003-3249-4431
Enrique Lopez-Rodriguez ● https://orcid.org/0000-0001-5357-6538
Rodion Stepanov ● https://orcid.org/0000-0001-8098-0720
Annie Hughes ● https://orcid.org/0000-0002-9181-1161
Konstantinos Tassis ● https://orcid.org/0000-0002-8831-2038
Susan E. Clark ● https://orcid.org/0000-0002-7633-3376
William T. Reach ● https://orcid.org/0000-0001-8362-4094
Julia Roman-Duval ● https://orcid.org/0000-0001-6326-7069
Le Ngoc Tram ● https://orcid.org/0000-0002-6488-8227
Ellen G. Zweibel ● https://orcid.org/0000-0003-4821-713X

References

Aller, L. H. 1958, AJ, 63, 47
Anaconda Software Distribution 2020, Anaconda Software Distribution, Vers. 2-2.4.0, Anaconda Inc., https://docs.anaconda.com/
Andersson, B. G., Lazarian, A., & Vaillancourt, J. E. 2015, ARA&A, 53, 501
Arshakian, T. G., Beck, R., Krause, M., & Sokoloff, D. 2009, A&A, 494, 21
Astropy Collaboration, Robitaille, T. P., Tollerud, E. J., et al. 2013, A&A, 558, A33
Battaner, E., & Florido, E. 2007, AN, 328, 92
Beck, R. 2015a, A&ARv, 24, 4
Beck, R. 2015b, A&A, 578, A93
Beck, R., Brandenburg, A., Moss, D., Shukurov, A., & Sokoloff, D. 1996, ARA&A, 34, 155
Beck, R., Chamandy, L., Elson, E., & Blackman, E. G. 2019, Galax, 8, 4
Beck, R., Klein, U., & Wielebinski, R. 1987, A&A, 186, 95
Beck, R., & Wielebinski, R. 2013, in Magnetic Fields in Galaxies, ed. T. D. Oswalt & G. Gilmore, Vol. 5 (Dordrecht: Springer), 641
Bendre, A., Gressel, O., & Elstner, D. 2015, AN, 336, 991
Berkhuijsen, E. M., Urbanik, M., Beck, R., & Han, J. L. 2016, A&A, 588, A114
Bolatto, A. D., Wolfire, M., & Leroy, A. K. 2013, ARA&A, 51, 207
Borlaff, A. 2021, Borlaff/M51_HAWC: Second Release, v2, Zenodo, doi:10.5281/zenodo.5116134
Borlaff, A., Eliche-Moral, M. C., Beckman, J. E., et al. 2017, A&A, 604, A119
Brandenburg, A., Sokoloff, D., & Subramanian, K. 2012, SSRv, 169, 123
Brandenburg, A., & Subramanian, K. 2005, PhR, 417, 1
Cabral, B., & Leedom, L. C. 1993, in Proc. 20th Annual Conf. on Computer Graphics and Interactive Techniques, SIGGRAPH '93 (New York,: Association for Computing Machinery), 263, doi:10.1145/166117.166151
Chyży, K. T., Sridhar, S. S., & Jurusik, W. 2017, A&A, 603, A121
Colombo, D., Meidt, S. E., Schinnerer, E., et al. 2014, ApJ, 784, 4
Davis, T. A., Alatalo, K., Bureau, M., et al. 2013, MNRAS, 429, 534
de Jong, T., Klein, U., Wielebinski, R., & Wunderlich, E. 1985, A&A, 147, L6
Dobbs, C. L., & Price, D. J. 2008, MNRAS, 383, 497
Dolginov, A. Z., & Mitrofanov, I. G. 1976, Ap&SS, 43, 291
Dowell, C. D., Cook, B. T., Harper, D. A., et al. 2010, Proc. SPIE, 7735, 77356H
Drzazga, R. T., Chyży, K. T., Jurusik, W., & Wiórkiewicz, K. 2011, A&A, 533, A22
Duc, P.-A., & Renaud, F. 2013, LNP, 861, 327
Elstner, D., Beck, R., & Gressel, O. 2014, A&A, 568, A104
Elvius, A. 1951, StoAn, 17, 4
Elvius, A., & Hall, J. S. 1964, LowOB, 6, 123
Fendt, C., Beck, R., & Neininger, N. 1998, A&A, 335, 123
Ferrière, K. M. 2001, RvMP, 73, 1031
Field, G. B., Goldsmith, D. W., & Habing, H. J. 1969, BAAS, 1, 240
Fissel, L. M., Ade, P. A. R., Angilè, F. E., et al. 2016, ApJ, 824, 134
Fissel, L. M., Ade, P. A. R., Angilè, F. E., et al. 2019, ApJ, 878, 110
Fletcher, A., Beck, R., Shukurov, A., Berkhuijsen, E. M., & Horellou, C. 2011, MNRAS, 412, 2396
Frick, P., Beck, R., Berkhuijsen, E. M., & Patrickeyev, I. 2001, MNRAS, 327, 1145
Frick, P., Stepanov, R., Beck, R., et al. 2016, A&A, 585, A21
Gent, F. A., Shukurov, A., Sarson, G. R., Fletcher, A., & Mantere, M. J. 2012, MNRAS Letters, 430, L40
Gnedin, N. Y., Ferrara, A., & Zweibel, E. G. 2000, ApJ, 539, 505
Gómez, G. C., Vázquez-Semadeni, E., & Zamora-Avilés, M. 2018, MNRAS, 480, 2939
Gordon, M. S., Lopez-Rodriguez, E., Andersson, B. G., et al. 2018, arXiv:1811.03100
Greaves, J. S., Holland, W. S., Jenness, T., & Hawarden, T. G. 2000, Natur, 404, 732
Gressel, O., Elstner, D., Ziegler, U., & Rüdiger, G. 2008a, A&A, 486, L35
Gressel, O., Ziegler, U., Elstner, D., & Rüdiger, G. 2008b, AN, 329, 619
Gunn, J. E., Siegmund, W. A., Mannery, E. J., et al. 2006, AJ, 131, 2332
Güver, T., & Özel, F. 2009, MNRAS, 400, 2050
Harper, D. A., Runyan, M. C., Dowell, C. D., et al. 2018, JAI, 7, 1840008
Haverkorn, M., Brown, J. C., Gaensler, B. M., & McClure-Griffiths, N. M. 2008, ApJ, 680, 362
Hoang, T., & Lazarian, A. 2014, MNRAS, 438, 680
Hoang, T., Tram, L. N., Lee, H., Diep, P. N., & Ngoc, N. B. 2021, ApJ, 908, 218
Horellou, C., Beck, R., Berkhuijsen, E. M., Krause, M., & Klein, U. 1992, A&A, 265, 417
Hughes, A., Meidt, S. E., Colombo, D., et al. 2013, ApJ, 779, 46
Hunter, D. A., Ficut-Vicas, D., Ashley, T., et al. 2012, AJ, 144, 134
Hunter, J. D. 2007, CSE, 9, 90
Iono, D., Yun, M. S., & Ho, P. T. P. 2005, ApJS, 158, 1
Jałocha, J., Bratek, Ł., Pękala, J., & Kutschera, M. 2012a, MNRAS, 421, 2155
Jałocha, J., Bratek, Ł., Pękala, J., & Kutschera, M. 2012b, MNRAS, 427, 393

Jones, T. J. 1997, AJ, 114, 1393
Jones, T. J. 2000, AJ, 120, 2920
Jones, T. J., Dowell, C. D., Lopez Rodriguez, E., et al. 2019, ApJL, 870, L9
Jones, T. J., Kim, J.-A., Dowell, C. D., et al. 2020, AJ, 160, 167
Kierdorf, M., Mao, S. A., Beck, R., et al. 2020, A&A, 642, A118
Kim, W.-T., & Stone, J. M. 2012, ApJ, 751, 124
Körtgen, B., Banerjee, R., Pudritz, R. E., & Schmidt, W. 2019, MNRAS, 489, 5004
Krause, M., Irwin, J., Schmidt, P., et al. 2020, A&A, 639, A112
Krause, M., Irwin, J., Wiegert, T., et al. 2018, A&A, 611, A72
Lazarian, A., & Hoang, T. 2007, MNRAS, 378, 910
Leroy, A. K., Sandstrom, K. M., Lang, D., et al. 2019, ApJS, 244, 24
Levy, R. C., Bolatto, A. D., Teuben, P., et al. 2018, ApJ, 860, 92
Lopez-Rodriguez, E. 2021, NatAs, 5, 604
Lopez-Rodriguez, E., Antonucci, R., Chary, R.-R., & Kishimoto, M. 2018, ApJL, 861, L23
Lopez-Rodriguez, E., Dowell, C. D., Jones, T. J., et al. 2020, ApJ, 888, 66
Lopez-Rodriguez, E., Guerra, J., Asgari-Targhi, M., & Schmelz, J. T. 2021, ApJ, 914, 24
Martin, D. C., Fanson, J., Schiminovich, D., et al. 2005, ApJL, 619, L1
Martin-Alvarez, S., Slyz, A., Devriendt, J., & Gómez-Guijarro, C. 2020, MNRAS, 495, 4475
Mathewson, D. S., van der Kruit, P. C., & Brouw, W. N. 1972, A&A, 17, 468
Matthews, B. C., McPhee, C. A., Fissel, L. M., & Curran, R. L. 2009, ApJS, 182, 143
McQuinn, K. B. W., Skillman, E. D., Dolphin, A. E., Berg, D., & Kennicutt, R. 2017, AJ, 154, 51
Mentuch Cooper, E., Wilson, C. D., Foyle, K., et al. 2012, ApJ, 755, 165
Mulcahy, D. D., Beck, R., & Heald, G. H. 2017, A&A, 600, A6
Neininger, N. 1992, A&A, 263, 30
Niklas, S., & Beck, R. 1997, A&A, 320, 54
Patrikeev, I., Fletcher, A., Stepanov, R., et al. 2006, A&A, 458, 441
Pavel, M. D., & Clemens, D. P. 2012, ApJL, 761, L28
Pety, J., Schinnerer, E., Leroy, A. K., et al. 2013, ApJ, 779, 43
Piddington, J. H. 1964, MNRAS, 128, 345
Pillai, T. 2017, arXiv:1711.00381
Pillai, T. G. S., Clemens, D. P., Reissl, S., et al. 2020, NatAs, 4, 1195
Planck Collaboration, Ade, P. A. R., Aghanim, N., et al. 2016, A&A, 586, A138

R Core Team 2020, R: A Language and Environment for Statistical Computing (Vienna: R Foundation for Statistical Computing)
Reback, J., McKinney, W., jbrockmendel, et al. 2021, pandas-dev/pandas: Pandas 1.2.3, v1.2.3, Zenodo, doi:10.5281/zenodo.4572994
Rees, M. J. 1987, QJRAS, 28, 197
Robitaille, T., & Bressert, E. 2012, APLpy: Astronomical Plotting Library in Python, Astrophysics Source Code Library, ascl:1208.017
Ruiz-Granados, B., Battaner, E., Calvo, J., Florido, E., & Rubiño-Martín, J. A. 2012, ApJL, 755, L23
Ruiz-Granados, B., Rubiño-Martín, J. A., Florido, E., & Battaner, E. 2010, ApJL, 723, L44
Sánchez-Salcedo, F. J., & Santillán, A. 2013, MNRAS, 433, 2172
Santos, F. P., Busquet, G., Franco, G. A. P., Girart, J. M., & Zhang, Q. 2016, ApJ, 832, 186
Scarrott, S. M., Ward-Thompson, D., & Warren-Smith, R. F. 1987, MNRAS, 224, 299
Schleicher, D. R. G., & Beck, R. 2013, A&A, 556, A142
Scholz, F. W., & Stephens, M. A. 1987, J. Am. Stat. Assoc., 82, 918
Segalovitz, A., Shane, W. W., & de Bruyn, A. G. 1976, Natur, 264, 222
Sokoloff, D. D., Bykov, A. A., Shukurov, A., et al. 1998, MNRAS, 299, 189
Soler, J. D., Ade, P. A. R., Angilè, F. E., et al. 2017, A&A, 603, A64
Subramanian, K. 2016, RPPh, 79, 076901
Sur, S., Basu, A., & Subramanian, K. 2021, MNRAS, 501, 3332
Tabatabaei, F. S., Martinsson, T. P. K., Knapen, J. H., et al. 2016, ApJL, 818, L10
Tabatabaei, F. S., Schinnerer, E., Murphy, E. J., et al. 2013, A&A, 552, A19
Tsiklauri, D. 2011, Ap&SS, 334, 165
Vaillancourt, J. E., Chuss, D. T., Crutcher, R. M., et al. 2007, Proc. SPIE, 6678, 66780D
van de Voort, F., Bieri, R., Pakmor, R., et al. 2021, MNRAS, 501, 4888
Van Eck, C. L., Brown, J. C., Shukurov, A., & Fletcher, A. 2015, ApJ, 799, 35
Van Rossum, G., & Drake, F. L., Jr. 1995, Python Reference Manual (Amsterdam: Centrum voor Wiskunde en Informatica)
Vollmer, B., Soida, M., Beck, R., et al. 2013, A&A, 553, A116
Walter, F., Brinks, E., de Blok, W. J. G., et al. 2008, AJ, 136, 2563
Wardle, J. F. C., & Kronberg, P. P. 1974, ApJ, 194, 249
Waskom, M., Gelbart, M., & Botvinnik, O. 2020, seaborn: statistical data visualization, Zenodo, doi:10.5281/zenodo.592845
Wright, E. L., Eisenhardt, P. R. M., Mainzer, A. K., et al. 2010, AJ, 140, 1868